PERGAMON

International Journal of Solids and Structures 36 (1999) 2641–2681

INTERNATIONAL JOURNAL OF SOLIDS and STRUCTURES

Postbuckling analysis and imperfection sensitivity of general shells by the finite element method

Mostafa Kheyrkhahan[a,*], Ralf Peek[b,1]

[a] *College of Engineering, The University of Michigan, Ann Arbor, MI 48109, U.S.A.*
[b] *Shell International Exploration and Production, Postbus 60, 2280 AB Rijswijk, The Netherlands*

Received 12 November 1996; in revised form 29 March 1998

Abstract

Buckling and imperfection sensitivity are the primary considerations in analysis and design of thin shell structures. The objective here is to develop accurate and efficient capabilities to predict the postbuckling behavior of shells, including imperfection sensitivity. The approach used is based on the Lyapunov–Schmidt–Koiter (LSK) decomposition and asymptotic expansion in conjunction with the finite element method. This LSK formulation for shells is derived and implemented in a finite element code. The method is applied to cylindrical and spherical shells. Cases of linear and nonlinear prebuckling behavior, coincident as well as non-coincident buckling modes, and modal interactions are studied. The results from the asymptotic analysis are compared to exact solutions obtained by numerically tracking the bifurcated equilibrium branches. The accuracy of the LSK asymptotic technique, its range of validity, and its limitations are illustrated.

Nomenclature

$\theta^1, \theta^2, \theta^3$	curvilinear coordinates
$(\cdot)_{,\alpha}$	$\partial(\cdot)/\partial\theta^\alpha$
$\mathbf{R}$	position vector of a point on the reference surface before deformation
$\tilde{\mathbf{R}}$	position vector of a point on a lamina before deformation
$\mathbf{D}$	director normal to the reference surface before deformation
ζ	scalar distance of a point on a lamina from the reference surface
$\mathbf{A}_\alpha$	tangent vector to the reference surface in the direction of θ^α before deformation
$\mathbf{G}_\alpha$	covariant basis vector in the direction of θ^α before deformation
$\mathbf{G}^\alpha$	contravariant basis vector (before deformation)

* Corresponding author
[1] Formerly at College of Engineering, The University of Michigan.

0020–7683/99/$ - see front matter
PII: S0020–7683(98)00129–2

$\mathbf{r}$	position vector of a point on the reference surface after deformation
$\tilde{\mathbf{r}}$	position vector of a point on a lamina after deformation
$\mathbf{d}$	director $\mathbf{D}$ after deformation
$\mathbf{a}_\alpha$	tangent vector to the reference surface in the direction of θ^α after deformation
$\mathbf{g}_\alpha$	covariant basis vector in the direction of θ^α after deformation
$\mathbf{g}^\alpha$	contravariant basis vector (after deformation)
$\mathbf{u}$	displacement of a point on the reference surface
$\tilde{\mathbf{u}}$	displacement of a point on a lamina
$\boldsymbol{\beta}$	$(\mathbf{d}-\mathbf{D})$ change in director

1. Introduction

Thin-walled structures are capable of carrying loads very efficiently. However, they are prone to buckling. They often have multiple, coincident or nearly coincident buckling modes, and can be very sensitive to imperfections. For such structures, even a small imperfection can produce a large drop in the load carrying capacity. In view of the above, the subject of shell stability always deserves rigorous attention and stability, not strength, is the more important factor in the design of shells.

This paper is a continuation of a previous effort by Peek and Kheyrkhahan (1993) to apply the Lyapunov–Schmidt–Koiter asymptotic approach in conjunction with the finite element method. This asymptotic approach was conceived by Koiter (1945) independently from the earlier work by the mathematicians Lyapunov and Schmidt (see e.g. Vainberg and Trenogin, 1962), to explain the high imperfection sensitivity of the buckling load of certain structures, such as cylindrical shells under axial compression.

Koiter's method is applicable for the case of a single buckling mode, or for multiple, fully coincident modes. The methodology was used in numerous analytical studies (see e.g. Amazigo et al., 1970; Budiansky, 1974; Hui and Du, 1987; Hutchinson and Amazigo, 1967; Hutchinson and Frauenthal, 1969; Rizzi and Tatone, 1985; Semenyuk, 1987) on postbuckling behavior and imperfection sensitivity of various structures for which the prebuckling solution and the buckling modes can be obtained analytically. For other structures, for which one has to resort to numerical methods, the singular asymptotic expansions have also proven useful (see e.g. Potier-Ferry, 1987; Carnoy, 1980).

For many structures and especially thin shells for which geometry and boundary conditions preclude inextensional deformations a large number of nearly coincident buckling modes occur. Koiter's version of the singular asymptotic expansions is not directly applicable for this case. In view of this, Byskov and Hutchinson (1977) developed an approach in which a number of nearly coincident or even non-coincident buckling modes can be included in the asymptotic analysis. Whereas their formulation of the asymptotics is limited to problems with linear prebuckling behavior, this restriction was removed in the work of Peek and Kheyrkhahan (1993), who generalized the LSK approach so that it could be applied to structures where the prebuckling behavior is nonlinear and at the same time the modes included in the asymptotic analysis need not be fully coincident.

Peek and Kheyrkhahan (1993) applied their generalized LSK asymptotic method to a variety

of simple one-dimensional structures, with a single buckling mode, or two fully coincident modes. The purpose of this paper is to apply the LSK approach to more realistic and complicated structures (shells), and to evaluate the effectiveness of the approach for the case when the modes are indeed not fully coincident.

2. The LSK asymptotic method

The theory of Lyapunov–Schmidt–Koiter decomposition and asymptotic expansions was discussed in detail in our previous work (see Peek and Kheyrkhahan, 1993). However, a brief description of the LSK technique seems necessary so that the readers can follow derivations of the LSK element, as well as subsequent asymptotic analyses.

Suppose that the structure considered is elastic with a potential energy function $\phi = \phi\ (u, \lambda, \bar{u})$ where u is the displacement field, λ is the load parameter, $\bar{u}$ represents an imperfection with $\bar{u} = 0$ corresponding to the perfect structure. The spaces of admissible displacement and imperfection fields are denoted by A and $\bar{A}$, respectively. A principal solution $\overset{0}{u}(\lambda)$ exists which vanishes at $\lambda = 0$ and satisfies the equilibrium condition

$$\phi_{,u}(\overset{0}{u}(\lambda), \lambda, 0)\, \delta u = 0 \quad \forall\, \delta u \in A, \quad \forall \lambda \tag{1}$$

where $(\cdot)_{,u}$ denotes a Gateaux (or Frechet) derivative. A reference point on the principal equilibrium branch is chosen, about which the asymptotic expansion is carried out. The value of the load parameter λ at the reference point is denoted by λ_c. In contrast to the classical analysis by Koiter (1945) in which the expansion is performed about a multiple bifurcation point, here the reference point need not coincide with any of the bifurcation points. Indeed any point on the principal equilibrium branch can be used as the reference point. The asymptotic expansion is valid in some neighborhood of the reference point whether the modes are fully coincident, closely spaced, or well separated. The space of admissible displacements A is decomposed into a subspace A_0, which is spanned by a finite number of modes $\overset{i}{\tilde{u}}$, and a complementary space $\hat{A}$ such that

$$A = A_0 \oplus \hat{A} \tag{2a}$$

$$A_0 \bigcap \hat{A} = \{0\} \tag{2b}$$

and there exists an $\alpha > 0$ such that

$$\phi^c_{,uu}\, \delta\hat{u}\, \delta\hat{u} \geqslant \alpha \quad \forall\, \delta\hat{u} \in \hat{A} \quad \text{with } \alpha > 0 \quad \text{and} \quad \|\delta\hat{u}\| = 1 \tag{3}$$

Equations (2) ensure that any displacement field $u \in A$ can be decomposed uniquely as

$$u = u_0 + \hat{u}, \quad u_0 \in A_0, \quad \hat{u} \in \hat{A} \tag{4a}$$

or

$$u = \sum_i \xi_i \overset{i}{\tilde{u}} + \hat{u}, \quad \hat{u} \in \hat{A} \tag{4b}$$

where ξ_i are scalar coefficients. Equation (3) ensures positive definiteness of the stability operator $\phi^c_{,uu}$ restricted to $\hat{A}$ in a nonvanishing neighborhood of the reference point. This decomposition

might be viewed by the finite element analyst as a nonlinear static condensation: one goes from a displacement field u (as described by all the nodal displacements and rotations) to a reduced set of degrees of freedom ξ_i which are chosen in such a way that for fixed ξ_i there can be no loss of stability.

The space $\hat{A}$ is often taken to be the orthogonal complement of A_0, but as was observed by Thompson and Hunt (1973), it is not necessary to introduce this restriction. Considerable flexibility also exists in the choice of the space A_0. For the case of fully coincident modes at $\lambda = \lambda_c$, the natural choice for A_0 is the nullspace of the stability operator evaluated at the reference point. In this case, the basis vectors $\tilde{u}$ satisfy

$$\phi^c_{,uu}\overset{i}{\tilde{u}}\,\delta u = 0 \quad \forall\, \delta u \in A \tag{5}$$

where a superscript c applied to the potential energy or any of its derivatives denotes evaluation at the reference point, $(u, \lambda, \bar{u}) = (\overset{0}{u}(\lambda_c), \lambda_c, 0)$. If the buckling modes are not fully coincident, then $\tilde{u}$ can be chosen as the eigenvectors corresponding to the smallest eigenvalues μ_i in

$$(\phi^c_{,uu} + \mu_i \dot{\phi}_{,uu})\overset{i}{\tilde{u}}\,\delta u = 0, \quad \forall\, \delta u \in A \tag{6}$$

where a dot placed above any entity denotes evaluation of that entity on the principal branch for the perfect structure, followed by differentiation with respect to λ, and evaluation at $\lambda = \lambda_c$. More generally, the modes $\tilde{u}$ need neither be chosen from equation (5) nor from eqn (6). Any set of linearly independent vectors can be chosen, as long as conditions (2) and (3) are satisfied (Peek and Kheyrkhahan, 1993). Applying the decomposition of eqn (4), displacements can be written as

$$u = \overset{0}{u}(\lambda) + \sum_j \xi_i \overset{i}{\tilde{u}} + \hat{u}, \quad \hat{u} \in \hat{A} \tag{7}$$

Correspondingly, the equilibrium conditions can be decomposed into the following two conditions

$$\phi_{,u}\left(\overset{0}{u}(\lambda) + \sum_j \overset{j}{\tilde{u}} + \hat{u}, \lambda, \varepsilon\bar{\bar{u}}\right)\delta\hat{u} = 0 \quad \forall\, \delta\hat{u} \in \hat{A} \tag{8}$$

$$\phi_{,u}\left(\overset{0}{u}(\lambda) + \sum_j \xi_j \overset{j}{\tilde{u}} + \hat{u}, \lambda, \varepsilon\bar{\bar{u}}\right)\overset{i}{\tilde{u}} = 0 \quad \forall\, i \tag{9}$$

In eqns (8) and (9), the imperfection has been written as $\bar{u} = \varepsilon\bar{\bar{u}}$, where $\bar{\bar{u}} \in \hat{A}$ is a normalized imperfection shape, and ε is the scalar magnitude of imperfection. The methodology is based on solving first equation (8) for $\hat{u}$, and then substituting the results into eqn (9) to obtain a reduced set of equilibrium equations for the modal displacement parameters ξ_i, which are then solved so that both equilibrium conditions are satisfied.

Equation (8) admits a unique solution $\hat{u} = \hat{u}(\xi_i, \lambda, \varepsilon) \in \hat{A}$ for any given $(\xi_i, \lambda, \varepsilon)$ in the vicinity of the reference point. The corresponding total displacement can be written as

$$u = u(\xi_i, \lambda, \varepsilon) \equiv \overset{0}{u}(\lambda) + \sum_j \xi_j \overset{j}{\tilde{u}} + \hat{u}(\xi_i, \lambda, \varepsilon) \tag{10}$$

The set of all such solutions is referred to as the partial equilibrium surface (see e.g. Thompson and Hunt, 1973; Peek and Kheyrkhahan, 1993). Differentiation of eqn (10) results in

$$u_{,i} = \overset{i}{\tilde{u}} + \hat{u}_{,i}, \quad u_{,\varepsilon} = \hat{u}_{,\varepsilon}, \quad u_{,ij} = \hat{u}_{,ij}, \quad u_{,i\lambda} = \hat{u}_{,i\lambda}, \text{etc.} \tag{11}$$

where $(\cdot)_{,i} \equiv \partial(\cdot)/\partial\xi_i$. The derivatives of the displacements with respect to parameters ξ_i, λ, and ε, evaluted at the reference point are denoted as follows

$$\overset{(i)}{u} \equiv [u_{,i}]_{(\xi_i,\lambda,\varepsilon)=(0,\lambda_c,0)}, \quad \overset{(\varepsilon)}{u} \equiv [u_{,\varepsilon}]_{(\xi_i,\lambda,\varepsilon)=(0,\lambda_c,0)}, \quad \overset{(ij)}{u} \equiv [u_{,ij}]_{(\xi_i,\lambda,\varepsilon)=(0,\lambda_c,0)} \tag{12}$$

$$\overset{(i)}{\hat{u}} \equiv [\hat{u}_{,i}]_{(\xi_i,\lambda,\varepsilon)=(0,\lambda_c,0)}, \quad \overset{(\varepsilon)}{\hat{u}} \equiv [\hat{u}_{,\varepsilon}]_{(\xi_i,\lambda,\varepsilon)=(0,\lambda_c,0)}, \quad \overset{(ij)}{\hat{u}} \equiv [\hat{u}_{,ij}]_{(\xi_i,\lambda,\varepsilon)=(0,\lambda_c,0)} \tag{13}$$

With the aid of eqn (10), eqn (8) can be rewritten as

$$\phi_{,u}(u(\xi_i,\lambda,\varepsilon),\lambda,\varepsilon\bar{\bar{u}})\,\delta\hat{u} = 0, \quad \forall\,\delta\hat{u}\in\hat{A}, \quad \forall(\xi_i,\lambda,\varepsilon) \tag{14}$$

Taking derivatives of this equation with respect to ξ_i, λ, and ε, and then evaluating the results at the reference point, produces

$$\phi^c_{,uu}\overset{(i)}{u}\,\delta\hat{u} = 0, \quad \forall\,\delta\hat{u}\in\hat{A} \tag{15}$$

$$(\phi^c_{,uu}\overset{(\lambda)}{u} + \phi^c_{,u\lambda})\,\delta\hat{u} = 0 \quad \forall\,\delta\hat{u}\in\hat{A} \tag{16}$$

$$(\phi^c_{,uu}\overset{(\varepsilon)}{u} + \phi^c_{,u\bar{\bar{u}}}\bar{\bar{u}})\,\delta\hat{u} = 0 \quad \forall\,\delta\hat{u}\in\hat{A} \tag{17}$$

$$(\phi^c_{,uu}\overset{(ij)}{u} + \phi^c_{,uuu}\overset{(i)}{u}\overset{(j)}{u})\,\delta\hat{u} = 0 \quad \forall\,\delta\hat{u}\in\hat{A} \tag{18}$$

$$(\phi^c_{,uu}\overset{(i\lambda)}{u} + \dot{\phi}_{,uu}\overset{(i)}{u})\,\delta\hat{u} = 0 \quad \forall\,\delta\hat{u}\in\hat{A} \tag{19}$$

It follows from eqns (15), (11), and (12) that

$$\overset{(i)}{u} = \overset{i}{\tilde{u}} + \overset{(i)}{\hat{u}} \tag{20}$$

$$\phi^c_{,uu}(\overset{i}{\tilde{u}} + \overset{(i)}{\hat{u}})\,\delta\hat{u} = 0 \quad \forall\,\delta\hat{u}\in\hat{A} \tag{21}$$

Equation (21) admits unique solutions for $\overset{(i)}{\hat{u}}\in\hat{A}$. Once this solution is available, $\overset{(i)}{u}$ can be calculated from eqn (20). It can be shown that the quantities $\overset{(\lambda)}{u}$, $\overset{(\lambda\lambda)}{u}$, and similar higher order derivatives are all zero (Peek and Kheyrkhahan, 1993). The unknown quantities $\overset{(\varepsilon)}{u}$, $\overset{(ij)}{u}$, $\overset{(i\lambda)}{u}$ are in space $\hat{A}$, and can be determined uniquely from eqns (17)–(19). Thus, an asymptotic expansion for the displacements on the partial equilibrium surface can be obtained as follows

$$u(\xi_i,\lambda,\varepsilon) = \overset{(0)}{u}(\lambda) + \sum_j \xi_i\overset{(i)}{u} + \Delta\lambda\dot{u} + \varepsilon\overset{(\varepsilon)}{u} + \frac{1}{2}\sum_{i,j}\xi_i\xi_j\overset{(ij)}{u} + \Delta\lambda\sum_i \xi_i\overset{(i\lambda)}{u} + \cdots \tag{22}$$

where $\Delta\lambda \equiv \lambda - \lambda_c$. Consider now the second equilibrium condition, eqn (9). If a reduced potential energy function is defined as

$$\psi(\xi_i, \lambda, \varepsilon) \equiv \phi(u(\xi_i, \lambda, \varepsilon), \lambda, \varepsilon\bar{\bar{u}}) \tag{23}$$

and this is differentiated with respect to ξ_i, one obtains

$$\psi_{,i} = \phi_{,u}(\overset{i}{\tilde{u}} + \hat{u}_{,i}) = \phi_{,u}\overset{i}{\tilde{u}} \tag{24}$$

Thus, stationarity of the reduced potential energy ($\psi_{,i} = 0$) is seen to be equivalent to the equilibrium condition (9). The equilibrium states are stable if and only if the matrix $\psi_{,ij}$ is positive definite (Triantafyllidis and Peek, 1992). Asymptotic expansion of eqn (24) about the reference point $(\xi_i, \lambda, \varepsilon) = (0, \lambda_c, 0)$ produces

$$\psi_{,i} = \varepsilon\phi_{i\varepsilon} + \sum_j \phi_{ij}\xi_j + \sum_j \phi_{ij\lambda}\xi_j\Delta\lambda + \frac{1}{2}\sum_{j,k}\phi_{ijk}\xi_j\xi_k + \sum_j \phi_{ij\varepsilon}\xi_j\varepsilon + \phi_{i\varepsilon\lambda}\varepsilon\,\Delta\lambda + \frac{1}{6}\sum_{j,k,l}\phi_{ijkl}\xi_j\xi_k\xi_l + \frac{1}{2}\sum_{j,k}\phi_{ijk\lambda}\xi_j\xi_k\,\Delta\lambda + \frac{1}{2}\sum_j \phi_{ij\lambda\lambda}\xi_j\,\Delta\lambda^2 + \cdots = 0 \tag{25}$$

The postbuckling coefficients $\phi_{i\varepsilon}$, ϕ_{ij}, $\phi_{ij\lambda}$, ϕ_{ijk}, etc. are derivatives of the reduced potential energy evaluated at the reference point. It follows from equilibrium at all points along the principal branch that the derivatives $\phi_{i\lambda}$, $\phi_{i\lambda\lambda}$, $\phi_{i\lambda\lambda\lambda}$, ... are all zero (Peek and Kheyrkhahan, 1993), so the corresponding terms are not shown in eqn (25). The expressions for other derivatives of the reduced potential energy can be simplified with the aid of eqn (15), to obtain

$$\phi_{i\varepsilon} = \phi^c_{,u\bar{u}}\overset{(i)}{\bar{\bar{u}}}u, \quad \phi_{ij} = \phi^c_{,uu}\overset{(i)(j)}{u\,u}, \quad \phi_{ij\lambda} = \dot{\phi}_{,uu}\overset{(i)(j)}{u\,u} \tag{26}$$

$$\phi_{ijk} = \phi^c_{,uuu}\overset{(i)(j)(k)}{u\,u\,u}, \quad \phi_{ij\varepsilon} = (\phi^c_{,uuu}\overset{(\varepsilon)}{u} + \phi^c_{,uu\bar{u}}\bar{\bar{u}})\overset{(i)(j)}{u\,u} \tag{27}$$

$$\phi_{i\varepsilon\lambda} = (\dot{\phi}_{,uu}\overset{(\varepsilon)}{u} + \dot{\phi}_{,u\bar{u}}\bar{\bar{u}})\overset{(i)}{u}, \quad \phi_{ij\lambda\lambda} = \ddot{\phi}_{,uu}\overset{(i)(j)}{u\,u} - 2\phi^c_{,uu}\overset{(i\lambda)(j\lambda)}{u\;\;u} \tag{28}$$

$$\phi_{ijkl} = \phi^c_{,uuuu}\overset{(i)(j)(k)(l)}{u\,u\,u\,u} - \phi^c_{,uu}(\overset{(il)(jk)}{u\;\;u} + \overset{(jl)(ik)}{u\;\;u} + \overset{(kl)(ij)}{u\;\;u}) \tag{29}$$

$$\phi_{ijk\lambda} = \dot{\phi}_{,uuu}\overset{(i)(j)(k)}{u\,u\,u} + \phi^c_{,uuu}(\overset{(i\lambda)(j)(k)}{u\,u\,u} + \overset{(j\lambda)(i)(k)}{u\,u\,u} + \overset{(k\lambda)(i)(j)}{u\,u\,u}) \tag{30}$$

The expansion in eqn (25) is valid no matter whether the modes are coincident, closely spaced, or well separated. Within this general framework, a variety of decompositions of the space of admissible displacements is possible, depending on the choice of the complementary space $\hat{A}$. The examples considered by Peek and Kheyrkhahan (1993) suggest that if $\hat{A}$ is chosen as the orthogonal complement of the space spanned by the buckling modes, the results are more accurate. This is the decomposition we use to obtain numerical results for shells.

In the case of fully coincident modes, asymptotic series solutions to eqn (25) can be obtained. For an asymmetric solution (i.e. when the coefficients ϕ_{ijk} are not all zero), the first term in the series (or leading order solution) is obtained by solving a truncated version of eqn (25), in which only the first four terms are included. In order to obtain the next higher order term in the series solutions the other terms shown in eqn (25) need to be considered as well. Indeed, simply solving (25) numerically (including only the terms shown) yields a solution with higher order accuracy

(i.e. the error in the solution of the truncated series for the equilibrium equations is of the same order as the error in a Taylor series expansion of the exact solution including the first two terms).

For a symmetric bifurcation the coefficients ϕ_{ijk} are all zero. Calculating the lowest possible order solution then requires the $\phi_{ijkl}\xi_j\xi_k\xi_l$ term in eqn (25) to be included in addition to the first three terms. In this case obtaining a solution with higher order accuracy would require including additional terms not shown in (25).

In the case of non-coincident modes, asymptotic series solutions can only be obtained if a mode splitting parameter is introduced (Peek and Kheyrkhahan, 1993; Triantafyllidis and Peek, 1992), whereby the structure is modified in such a way that for a zero value of the mode splitting parameter, the modes are fully coincident. In the asymptotic series solutions that then arise, the mode splitting parameter is also expanded in terms of the solution parameter ξ. As a result the solutions calculated from the series expansion correspond not to different solutions for a given structure, but rather to different solutions for different structures. Since in the examples given attention is focused on one given structure at a time, the mode splitting parameter is not used here. However it is clear from the mode slitting formalism, that although the series expansion of the reduced equilibrium eqn (25) is valid no matter whether the modes are coincident, closely spaced, or well separated, the asymptotic solutions to this series will in general have a limited range of validity. This range of validity must extend to a value of the mode splitting parameter that describes the actual structure to be analyzed. Consequently, solutions to the truncated series version of (25) will in general only be valid if the modes are sufficiently closely spaced. How close this must be is investigated in the examples that follow.

3. The LSK shell element

In a conventional nonlinear finite element code, calculations at the element level are limited to computing the tangent stiffness, the element loads and the out-of-balance nodal forces. However, the 'Lyapunov–Schmidt–Koiter' decomposition and asymptotic expansion technique requires that certain higher order derivatives of the potential function be computed as well. The dot products of the third and fourth variation of the potential function with the given vectors [corrected buckling modes given by eqn (20)] have to be calculated. In this section the general formulations of the 'LSK' shell element are presented. The goal here is to provide an overview of the procedures involved in developing the LSK shell element. Algebraic derivations are included only to the extent that is needed for clarity.

Calculation of the tangent stiffness matrix depends on the relations between strains and displacements. We would like to develop a small strain, large deformation shell element. The first step is to establish the strain–displacement relations.

3.1. Shell kinematics and discretization

Shell theories for use in finite element applications has been an area of continuing development (see e.g. Ibrahimbegovic, 1994; Ibrahimbegovic and Frey, 1994; Basar and Ding, 1995, 1996; Buchter and Ramm, 1992; Buchter et al., 1994; Simo and Fox, 1989). The intent here is not to

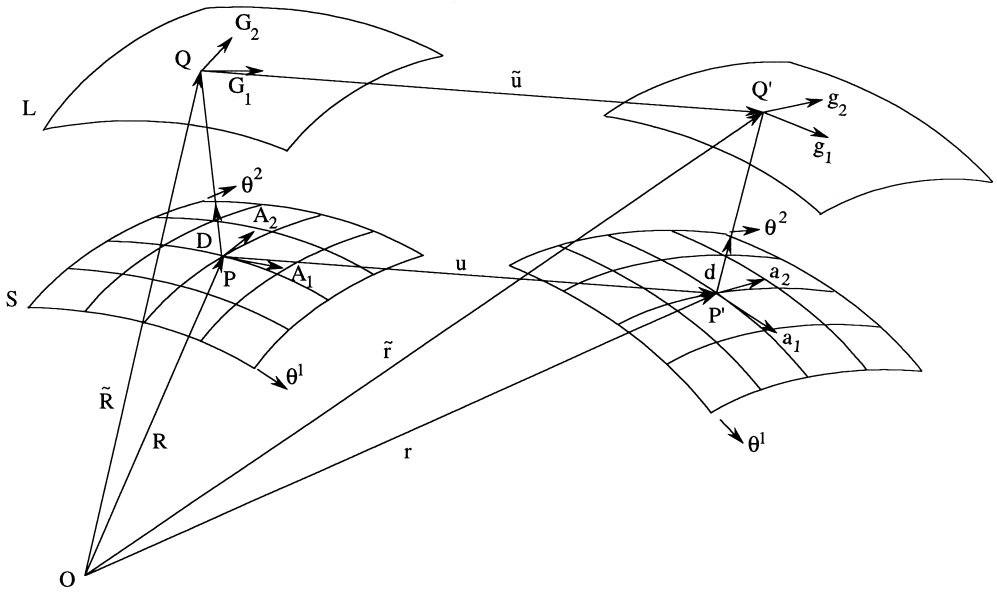

Fig. 1. Geometry of the shell before and after deformation.

develop a new shell theory, but rather to use a simple and reliable displacement-based approach. For this purpose the following assumptions are made:

(i) the displacements and rotations may be arbitrarily large, but the strains are small;
(ii) material fibers which are (approximately) normal to the reference surface remain straight and inextensional during deformation, but shear deformations by which the fibers can rotate with respect to the reference surface are allowed;
(iii) the material behavior is linearly elastic;
(iv) the normal stress (i.e. normal component of traction acting on a surface parallel to the reference surface) is assumed to be zero for the purpose of determining the relationship between the other stress and strain components, and
(v) for the purpose of integrating the strain energy across the thickness of the shell, the strain tensor is firt expressed in terms of orthonormal basis vectors that do not depend on the across-thickness coordinate, retaining only the constant and the first order terms in a Taylor series expansion of these strain components across the thickness; then integration across the thickness is performed analytically, neglecting any difference in area between an infinitesimal element of a lamina away from the reference surface and the corresponding infinitesimal element on the reference surface (as projected by the directors).

The geometry of the shell before and after deformation is illustrated in Fig. 1. Therein (θ^1, θ^2) are the surface coordinates defining a point on the reference surface S, with the position vector of a point on this reference surface being denoted by $\mathbf{R} = \mathbf{R}(\theta^1, \theta^2)$ before deformation, and $\mathbf{r} = \mathbf{r}(\theta^1, \theta^2)$ after deformation. The across-thickness coordinate θ^3 identifies different laminae L of the shell, with the position vector of a point on a lamina being denoted by $\tilde{\mathbf{R}} = \tilde{\mathbf{R}}(\theta^1, \theta^2, \theta^3)$ before defor-

mation, and by $\tilde{\mathbf{r}} = \tilde{\mathbf{r}}(\theta^1, \theta^2, \theta^3)$ after deformation. Also shown in Fig. 1 are covariant basis vectors, tangent vectors, and directors defined by:

Undeformed configuration:

$$\begin{aligned}\tilde{\mathbf{R}}(\theta^1, \theta^2, \theta^3) &= \mathbf{R}(\theta^1, \theta^2) + \zeta \mathbf{D}(\theta^1, \theta^2) \quad \theta^3 = \zeta \\ &\mathbf{G}_i \equiv \tilde{\mathbf{R}}_{,i} \quad \mathbf{G}_3 \equiv \mathbf{D} \quad \mathbf{A}_\alpha \equiv \mathbf{R}_{,\alpha} \quad i = 1,2,3, \quad \alpha = 1,2 \\ &\mathbf{G}_\alpha = \mathbf{R}_{,\alpha} + \zeta \mathbf{D}_{,\alpha} = \mathbf{A}_\alpha + \zeta \mathbf{D}_{,\alpha} \quad \alpha = 1,2 \end{aligned} \tag{31}$$

Deformed configuration:

$$\begin{aligned}\hat{\mathbf{r}}(\theta^1, \theta^2, \theta^3) &= \mathbf{r}(\theta^1, \theta^2) + \zeta \mathbf{d}(\theta^1, \theta^2) \quad \theta^3 = \zeta \\ &\mathbf{g}_i \equiv \tilde{\mathbf{r}}_{,i} \quad \mathbf{g}_3 \equiv \mathbf{d} \quad \mathbf{a}_\alpha \equiv \mathbf{r}_{,\alpha} \quad i = 1,2,3, \quad \alpha = 1,2 \\ &\mathbf{g}_\alpha = \mathbf{r}_{,\alpha} + \zeta \mathbf{d}_{,\alpha} = \mathbf{a}_\alpha + \zeta \mathbf{d}_{,\alpha} \quad \alpha = 1,2 \end{aligned} \tag{32}$$

In the finite element discretization the coordinates and the directors are interpolated from nodal values, in the deformed as well as the undeformed configurations. As a result the interpolated directors will not be exactly normal to the reference surface (i.e. $\mathbf{A}_\alpha \cdot \mathbf{D} \neq 0$), nor will they have a magnitude of precisely one. On the other hand, the coordinates (θ_1, θ_2) will be chosen in such a way that $\mathbf{A}_1$ and $\mathbf{A}_2$ are orthonormal with respect to each other at the Gaussian integration points where the strain energy is evaluated. This can readily be achieved, since different coordinates θ_1 and θ_2 can be chosen for every Gaussian integration point in question.

Referring to Fig. 1, the displacement of a typical point P on a lamina is

$$\tilde{\mathbf{u}} = \mathbf{u} + \zeta \boldsymbol{\beta} \tag{33}$$

where

$$\boldsymbol{\beta} = \mathbf{d} - \mathbf{D} \tag{34}$$

is the change in the director. The relations between tangent vectors and the covariant basis vectors in the deformed and undeformed configurations are found as follows

$$\mathbf{r} = \mathbf{R} + \mathbf{u} \quad \tilde{\mathbf{r}} = \tilde{\mathbf{R}} + \tilde{\mathbf{u}} \tag{35}$$

$$\mathbf{r}_{,\alpha} = \mathbf{R}_{,\alpha} + \mathbf{u}_{,\alpha} \Rightarrow \mathbf{a}_\alpha = \mathbf{A}_\alpha + \mathbf{u}_{,\alpha} \tag{36}$$

$$\tilde{\mathbf{r}}_{,\alpha} = \tilde{\mathbf{R}}_{,\alpha} + \tilde{\mathbf{u}}_{,\alpha} \Rightarrow \mathbf{g}_\alpha = \mathbf{G}_\alpha + \tilde{\mathbf{u}}_{,\alpha} \tag{37}$$

Substitution of equation (33) in the above results in

$$\mathbf{g}_\alpha = \mathbf{G}_\alpha + \mathbf{u}_{,\alpha} + \zeta \boldsymbol{\beta}_{,\alpha} \tag{38}$$

3.2. Strain–displacement relations

The Green–Lagrange strain tensor is

$$\mathbf{E} = E_{ij} \mathbf{G}^i \mathbf{G}^j \quad i,j = 1,2,3 \tag{39}$$

The strain components E_{ij} are obtained from

$$E_{ij} = \tfrac{1}{2}(g_{ij} - G_{ij}) \tag{40}$$

where g_{ij} and G_{ij} are metric tensors. The strain tensor can be expanded as follows:

$$\mathbf{E} = E_{\alpha\beta}\mathbf{G}^{\alpha}\mathbf{G}^{\beta} + E_{\alpha 3}(\mathbf{G}^{\alpha}\mathbf{G}^{3} + \mathbf{G}^{3}\mathbf{G}^{\alpha}) + E_{33}\mathbf{G}^{3}\mathbf{G}^{3} \quad \alpha, \beta = 1, 2 \tag{41}$$

where $E_{\alpha\beta}$ represent in-plane components. The components of in-plane strain tensor given by Kheyrkhahan (1995) are:

$$E_{\alpha\beta} = e_{\alpha\beta} + \zeta\kappa_{\alpha\beta} + O(\zeta^2) \tag{42}$$

where

$$e_{\alpha\beta} = \tfrac{1}{2}[\mathbf{A}_{\alpha} \cdot \mathbf{u}_{,\beta} + \mathbf{u}_{,\alpha} \cdot \mathbf{A}_{\beta} + \mathbf{u}_{,\alpha} \cdot \mathbf{u}_{,\beta}] \quad \alpha, \beta = 1, 2 \tag{43}$$

and

$$\kappa_{\alpha\beta} = \tfrac{1}{2}[\mathbf{D}_{,\alpha} \cdot \mathbf{u}_{,\beta} + \mathbf{u}_{,\alpha} \cdot \mathbf{D}_{,\beta} + \mathbf{A}_{\alpha} \cdot \boldsymbol{\beta}_{,\beta} + \boldsymbol{\beta}_{,\alpha} \cdot \mathbf{A}_{\beta} + \mathbf{u}_{,\alpha} \cdot \boldsymbol{\beta}_{,\beta} + \boldsymbol{\beta}_{,\alpha} \cdot \mathbf{u}_{,\beta}] \tag{44}$$

Calculation of in-plane strain tensor ($\mathbf{E} = E_{\alpha\beta}\mathbf{G}^{\alpha}\mathbf{G}^{\beta}$), involves multiplication by the contravariant basis vectors $\mathbf{G}^{\alpha}$ and $\mathbf{G}^{\beta}$. Kheyrkhahan (1995) calculated these basis vectors and showed that

$$\mathbf{E} = (e_{\alpha\beta} + \zeta\mathbf{K}_{\alpha\beta} + O(\zeta^2))\mathbf{A}^{\alpha}\mathbf{A}^{\beta} \tag{45}$$

where $e_{\alpha\beta}$ is given in eqn (43), and $\mathbf{K}_{\alpha\beta}$ is as follows

$$\mathbf{K}_{\alpha\beta} = (\kappa_{\alpha\beta} + e_{\alpha\gamma}B^{\gamma}_{\beta} + e_{\beta\gamma}B^{\gamma}_{\alpha}) \tag{46}$$

In the above relation $\kappa_{\alpha\beta}$ is the same as eqn (44), while quantities B^{γ}_{β}, and the like are defined by

$$B^{\gamma}_{\beta} = -\mathbf{A}^{\gamma} \cdot \mathbf{D}_{,\beta} \tag{47}$$

The transverse shear components of the Green–Lagrange strain tensor defined in (39) are given by

$$E_{\alpha 3} = \tfrac{1}{2}(\mathbf{g}_{\alpha} \cdot \mathbf{g}_{3} - \mathbf{G}_{\alpha} \cdot \mathbf{G}_{3}) \quad \alpha = 1, 2 \tag{48}$$

Substitution of previous equations in the above and further simplification (see Kheyrkhahan, 1995) results in

$$E_{\alpha 3} = e_{\alpha 3} + O(\zeta) \tag{49}$$

where

$$e_{\alpha 3} = \tfrac{1}{2}(\mathbf{A}_{\alpha} \cdot \boldsymbol{\beta} + \mathbf{u}_{,\alpha} \cdot \mathbf{D} + \mathbf{u}_{,\alpha} \cdot \boldsymbol{\beta}) \quad \alpha = 1, 2 \tag{50}$$

The directors have been defined as material fibers that remain straight, but so far there is no requirement as to normality, neither in the undeformed nor the deformed configuration. Indeed in the approach used the coordinates θ^1 and θ^2 will be chosen in such a way that the vectors tangent to the reference surface, $\mathbf{A}_{\alpha}$ are orthonormal with respect to each other, but only approximately orthogonal to the director $\mathbf{D}$. Therefore, the strain tensor components $E_{\alpha 3}$ do not bear a direct physical interpretation as a change in angle between two originally orthogonal material lines, even for small strains. Rather, for the case that $\mathbf{A}_{\alpha}$ are orthonormal, this change in angle is given by

$$\gamma_\alpha = \frac{2}{\|\mathbf{A}^3\|} E_{\alpha j} A^{j3} \tag{51}$$

More precisely, for small strains, γ_α represents the change in angle between the tangent to the reference surface along the θ_α coordinate direction, and the normal to the reference surface. In eqn (51) A^{j3} are the contravariant components of the metric tensor given by

$$[A^{ij}] = [A_{ij}]^{-1} = \frac{1}{1-\alpha_1^2-\alpha_2^2}\begin{bmatrix} 1-\alpha_2^2 & \alpha_1\alpha_2 & -\alpha_1 \\ \alpha_1\alpha_2 & 1-\alpha_1^2 & -\alpha_2 \\ -\alpha_1 & -\alpha_2 & 1 \end{bmatrix} \tag{52}$$

where

$$[A_{ij}] = \begin{bmatrix} 1 & 0 & \alpha_1 \\ 0 & 1 & \alpha_2 \\ \alpha_1 & \alpha_2 & 1 \end{bmatrix}, \quad \alpha_\alpha = \mathbf{A}_\alpha \cdot \mathbf{D}, \quad \mathbf{D} = \mathbf{A}_3 \tag{53}$$

and $\mathbf{A}^3 = A^{3j}\,\mathbf{A}_j$ is a vector normal to the reference surface.

3.3. Potential function

The potential function ϕ of a finite element is given by

$$\phi = \frac{1}{2}\int_\Omega \varepsilon^{\mathrm{T}} \sigma \, \mathrm{d}\Omega \tag{54}$$

where ε is the strain vector, and σ represents the stress resultants. Integration is carried out on the element domain Ω. The strain vector is composed of three membrane strains, three curvature changes, and two transverse shear strains;

$$\varepsilon^{\mathrm{T}} = \{e_{11} \quad e_{22} \quad 2e_{12} \quad K_{11} \quad K_{22} \quad 2K_{12} \quad \gamma_1 \quad \gamma_2\} \tag{55}$$

Correspondingly, the stress resultants are three membrane forces, three bending moments, and two shears.

$$\sigma^{\mathrm{T}} = \{N_{11} \quad N_{22} \quad N_{12} \quad M_{11} \quad M_{22} \quad M_{12} \quad Q_1 \quad Q_2\} \tag{56}$$

The in-plane strains e_{11}, e_{22}, and e_{12}, are determined from eqn (43). Changes in the curvature K_{11}, K_{22}, and K_{12} are found from eqn (46), and the shear strains γ_1 and γ_2 are calculated from eqn (51).

The stresses and strains are related by the tangent material matrix $\bar{\mathbf{D}}$.

$$\boldsymbol{\sigma} = \bar{\mathbf{D}}\varepsilon \quad \text{where } \bar{\mathbf{D}} = \begin{bmatrix} \mathbf{D}_m & 0 & 0 \\ 0 & \mathbf{D}_b & 0 \\ 0 & 0 & \mathbf{D}_s \end{bmatrix} \tag{57}$$

The submatrices $\mathbf{D}_m$, $\mathbf{D}_b$, and $\mathbf{D}_s$ correspond to membrane, bending, and shear respectively, and are defined by

$$\mathbf{D}_m = \frac{Eh}{1-v^2}\begin{bmatrix} 1 & v & 0 \\ v & 1 & 0 \\ 0 & 0 & \dfrac{1-v}{2} \end{bmatrix} \quad \mathbf{D}_b = \frac{h^2}{12}\mathbf{D}_m \quad \mathbf{D}_s = cGh\begin{bmatrix} 1 & 0 \\ 0 & 1 \end{bmatrix} \tag{58}$$

In the above, v is the Poisson ratio, E is the modulus of elasticity, and G is the shear modulus $G = E/(2+2v)$.

The factor c is introduced to account for out-of-straight deformations of the fibers. A value of $c = 1$ is consistent with the assumption that straight fibers remain straight. However, this assumption implies a constant distribution of shear stress across the thickness, which violates the condition that the shear stress must vanish at the surfaces of the shell. The actual distribution of shear stresses is closer to parabolic, corresponding to an S-shaped deformation of the fibers. For this a value of $c = 5/6$ is appropriate, which is the value used in all the examples presented here.

Within the shell element a nine-node isoparametric formulation is used to interpolate from the nodal values of the displacements and directors. Membrane and shear locking is avoided by the use of selective reduced integration.

The LSK formulation requires calculation of the derivatives of the element potential energy up to the fourth order with respect to the nodal displacements. This differentiation process is carried out fully analytically, resulting, in some lengthy expressions, which are given by Kheyrkhahan (1995), but not reproduced here for the sake of brevity. The needed derivatives of the potential energy with respect to nodal coordinates are also evaluated analytically by Kheyrkhahan (1995). These are used in the imperfection sensitivity calculations presented here.

Pressure loads acting on the shell surface, and their contribution to the derivatives of the potential energy are also included. Although on a single element level, the pressure loads are non-conservative, in most physically realistic situations the pressure load does become a conservative load when one considers the system as a whole. (The potential of the pressure load is the pressure multiplied by the change of volume contained by the shell.) This also applies to the spherical cap problem with external pressure presented here. The formulation for element pressure loads used here is such that (i) it results in symmetric contribution to the element tangent stiffness matrix, and (ii) it gives the proper pressure potential for the system as a whole, when the pressure loading is conservative. This is achieved by writing the change in volume contained by the shell as a sum of element contributions, which then gives rise to the element contributions to the pressure potential (see Kheyrkhahan, 1995).

3.4. Example 1: Cylinder with two coincident modes under axial load

Consider a cylinder of length l under axial loading between lubricated rigid end plates. Such lubricated rigid end plates restrain the displacement component normal to the end plate (both into or out of the plate) at all points across the thickness of the shell, but the component of displacement tangential to the lubricated plate is not restrained. (Thus, rotation of the director is restrained about an axis in the circumferential direction, but unrestrained about an axis in the axial direction of the shell.) According to the classical analysis based on the Donnel, Von Karman, Vlasov moderate deflection shell theory, the buckling modes involve a sinusoidal shape in the axial as well as circumferential direction, and the corresponding axial buckling stresses are given by:

$$\lambda = \frac{1}{2}\sigma_{cl}\left(C + \frac{1}{C}\right) \tag{59}$$

where

$$\sigma_{cl} = \frac{Eh}{R\sqrt{3(1-\nu^2)}} \tag{60}$$

and

$$C = \frac{\beta_1^2}{[\beta_1^2 + \beta_2^2]^2} \tag{61}$$

In the above equations E is the modulus of elasticity, ν is the Poisson ratio, and h is the shell thickness. In addition R is the radius, while β_1 and β_2 are dimensionless wavenumbers given by

$$\begin{cases} \beta_1 = \dfrac{l_0}{l_1} = \dfrac{ml_0}{l} \\ \beta_2 = \dfrac{l_0}{l_2} = \dfrac{nl_0}{\pi R} \end{cases}, \quad \begin{cases} l_1 = \dfrac{l}{m} \\ l_2 = \dfrac{\pi R}{n} \end{cases} \tag{62}$$

In the above relations m and $2n$ are the number of half waves involved in the buckling mode for the axial and circumferential directions, respectively; l_1 and l_2 are the corresponding half-wavelengths; and l_0 is a reference half wavelength (half wavelength of the axisymmetric mode with the lowest buckling load) given by

$$l_0 = \frac{\pi\sqrt{Rh}}{[12(1-\nu^2)]^{1/4}} \tag{63}$$

The buckling load λ given by eqn (59) is minimized when $C = 1$. In this case eqn (61) becomes

$$(\beta_1 - \tfrac{1}{2})^2 + \beta_2^2 = (\tfrac{1}{2})^2 \tag{64}$$

which represents the Koiter's circle (Fig. 2). The points on Koiter's circle correspond to buckling modes for which the critical load is a minimum. However, boundary conditions dictate that only discrete values of β_1 and β_2 are possible corresponding to integer values of m and n [see eqn (62)]. This gives rise to a grid of points corresponding to possible values of β_1 and β_2. The points falling closest to Koiter's circle will correspond to the lowest buckling loads. (More precisely, the contours of constant buckling load in the β_1, β_2 wavenumber space are circles which are tangent to Koiter's circle at the origin.)

By appropriate choice of the problem parameters one can ensure that the grid of possible buckling modes on the Koiter's circle includes modes at points $(1, 0)$ and $(1/2, 1/2)$. These are shown as points A and B in Fig. 2. They correspond to two fully coincident buckling modes at the lowest possible bifurcation load. Point A corresponds to an axisymmetric mode shown in Fig. 3a. The length of the cylinder is chosen such that this mode involves two half waves in the axial direction (i.e. $m = 2$).

In regard to the circumferential direction, the thickness of the cylinder is chosen so that the

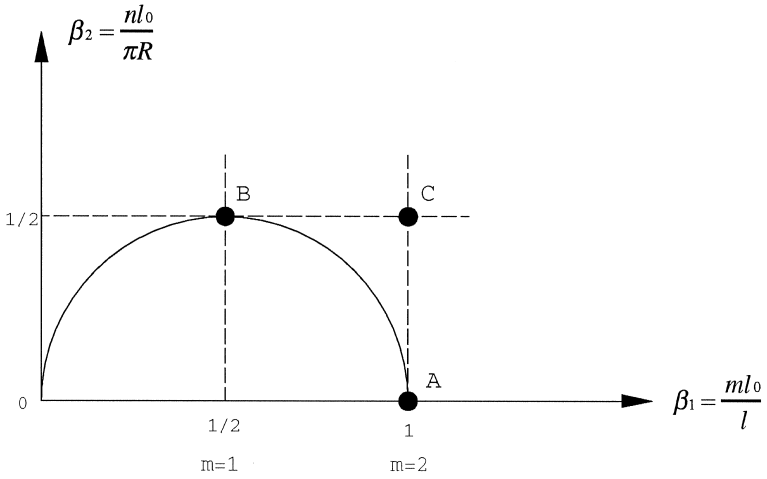

Fig. 2. The Koiter's circle, the grid shown corresponds to two coincident buckling modes.

mode at B (Fig. 2) corresponds to a mode involving 24 full waves in the circumferential direction (i.e. $n = 24$). This mode is illustrated in Fig. 3b. For the full cylinder, a large number of closely spaced modes with nearby values of n would be possible. However, to reduce the number of possible modes, attention is focused on a cylindrical panel with symmetry boundary conditions at the ends, rather than on the full cylinder. The width of the panel is taken to be one 48th of the circumference, so that the mode corresponding to point B in Fig. 2 (or mode 2 in Fig. 3) involves one half wavelength over the width of the panel. This means that the modes that are possible for the panel are also modes for the cylindrical shell with $(n = 0, 24, 48, 72, \ldots.)$. Thus, the solutions for the cylindrical panel problem (Fig. 4) also correspond to solutions for the full cylinder, but for the full cylinder there may be additional solutions (corresponding for instance to secondary bifurcations) that are not present in the cylindrical panel problem.

In the finite element analysis, the cylindrical panel is discretized into 16 nine-node shell elements. This implies an element length of one quarter of the minimum buckling wavelength in the axial direction, and one eighth the minimum buckling wavelength in the circumferential direction. A converged solution is obtained on the principal branch at a reference point which is very close to the bifurcation point (0.997). Since the stability operator $\phi^c_{,uu}$ loses its positive definiteness at the critical point, we cannot get a converged solution exactly at $\lambda = 1.0$. However, the reference point does not have to coincide with the bifurcation point (Peek and Kheyrkhahan, 1993). The first and the second buckling modes of the complete cylinder as obtained from the finite element solution are shown in Fig. 3.

Evaluation of the third order postbuckling coefficients ϕ_{ijk} using the finite element based approach yields zero for all postbuckling coefficients, except for $\phi_{122} = \phi_{212} = \phi_{221}$. With proper normalization of the modes the asymptotic expansion of the reduced equilibrium equations results in

$$\begin{cases} -\Delta\lambda\xi_1 + \frac{1}{2}\phi_{122}\xi_2^2 + \cdots = 0 \\ -\Delta\lambda\xi_2 + \phi_{122}\xi_1\xi_2 + \cdots = 0 \end{cases} \tag{65}$$

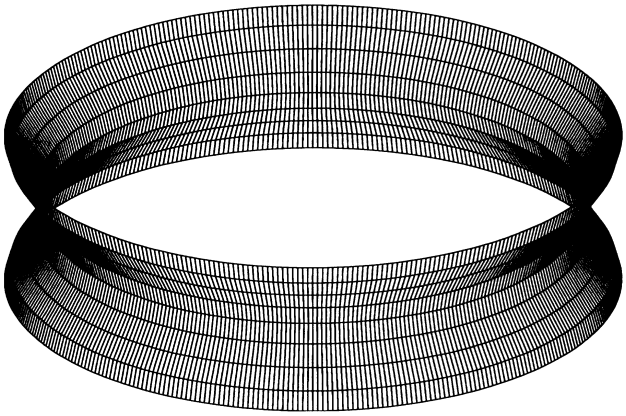

(a) First buckling mode

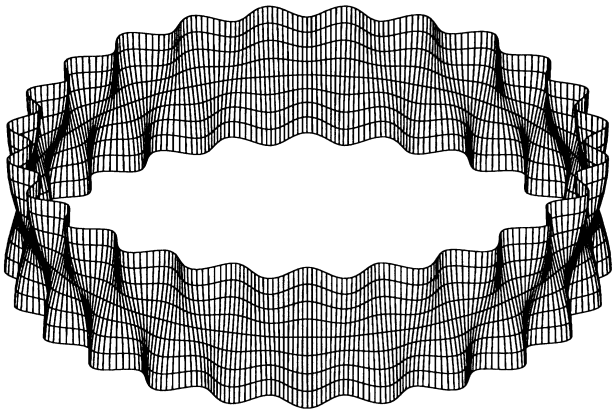

(b) Second buckling mode

Fig. 3. The buckling modes of a cylinder subjected to axial load.

for which the bifurcated solution can be written as

$$\xi_1 = \xi + O(\xi^2), \quad \xi_2 = O(\xi^2), \quad \lambda = \lambda_c + O(\xi^2)$$
$$\xi_1 = -\sqrt{1/3}\xi + O(\xi^2), \quad \xi_2 = \pm\sqrt{2/3}\xi + O(\xi^2), \quad \lambda = \lambda_c + \bar{\lambda}_1\xi + O(\xi^2) \tag{66}$$

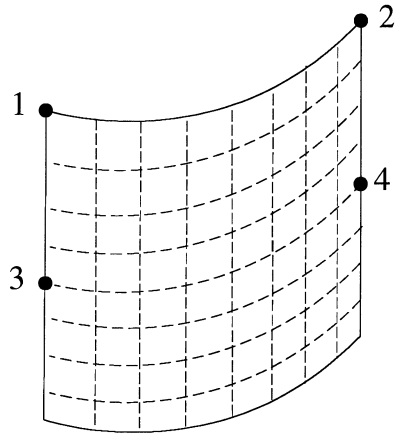

Fig. 4. The cylindrical panel and the nodal points which are used to define the buckling deflections.

where $\bar{\lambda}_1 = -\phi_{122}/\sqrt{3}$ and ξ is a solution parameter, which can assume positive or negative values. Thus there are a total of three bifurcated solution branches through the multiple bifurcation point. The solution above, without the higher order terms, will be referred to as the leading order solution. A higher order accurate solution may be obtained by including also the ϕ_{ijkl} term in the truncated series of the reduced equilibrium equations (Peek and Kheyrkhahan, 1993), and solving the resulting equations numerically, to obtain higher order accurate values of ξ_1, ξ_2, and λ. Higher order accurate values of the displacements are then obtained from

$$u = \overset{0}{u}(\lambda) + \sum_{i=1}^{m} \xi_i \overset{i}{\tilde{u}} + \frac{1}{2} \sum_{i=1}^{m} \sum_{j=1}^{m} \xi_i \xi_j \overset{(ij)}{u} \tag{67}$$

This higher order accurate solution is illustrated in Fig. 5 together with the leading order solution, and the exact solution, computed by numerically tracking the bifurcated solution branches. The buckling displacements shown in Fig. 5 are defined as

$$u_1 = \tfrac{1}{4}(w_1 + w_2 - w_3 - w_4), \quad u_2 = \tfrac{1}{2}(w_2 - w_1) \tag{68}$$

where w_i refers to the transverse displacement at the node labeled i in Fig. 4. This definition ensures that the first buckling mode contributes only to buckling displacement u_1, and the second buckling mode only to buckling displacement u_2. Another view of the bifurcation diagram can be obtained by plotting the load as a function of end shortening (Fig. 6). As can be seen inclusion of the higher order term increases accuracy and the results follow the exact solution up to 25% load drop.

So far the solutions for the perfect structure have been investigated. Consider now a cylinder with a geometric imperfection that is a linear combination of the buckling modes, in the form

$$\bar{u} = \varepsilon(\bar{\alpha}_1 \overset{1}{\tilde{u}} + \bar{\alpha}_2 \overset{2}{\tilde{u}}) \tag{69}$$

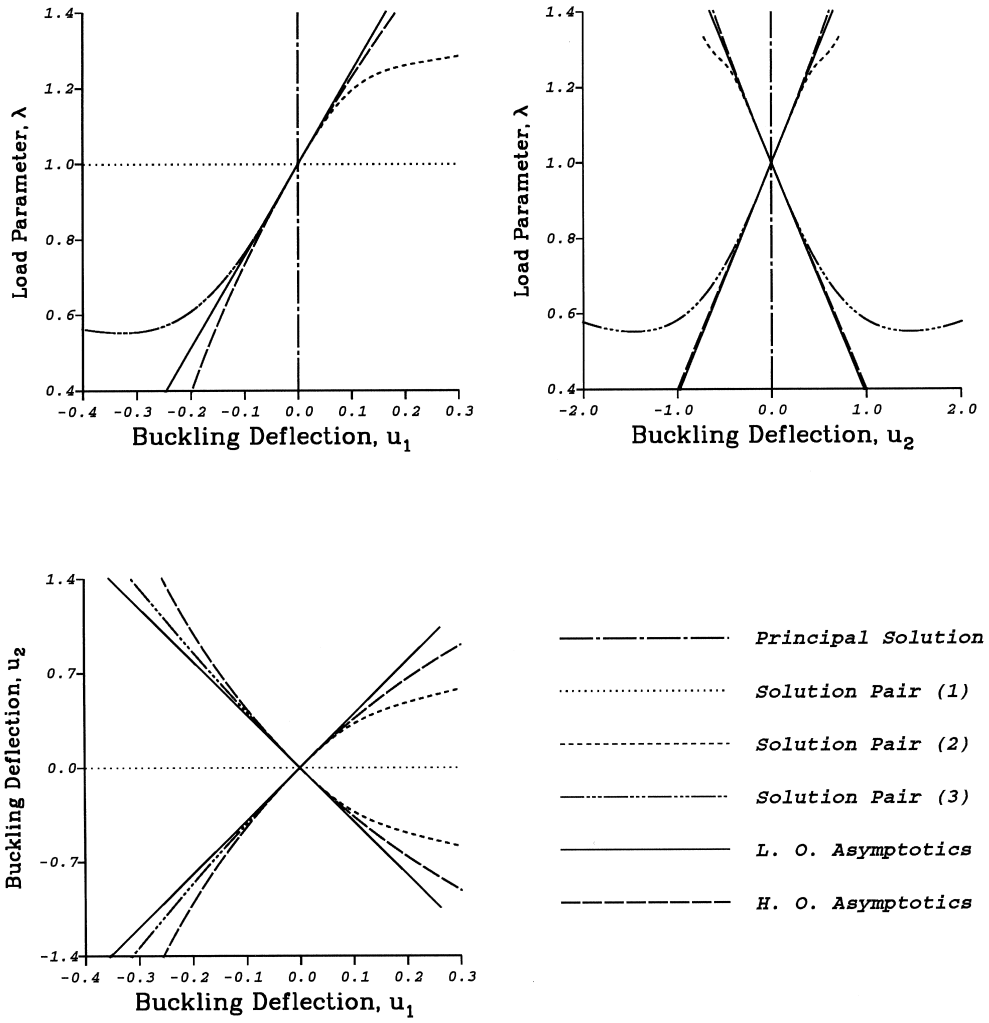

Fig. 5. Bifurcation diagrams of a cylindrical panel subjected to axial load.

where ε is the imperfection amplitude, and $\bar{\alpha}_1$ and $\bar{\alpha}_2$ describe the direction of the imperfection with $\bar{\alpha}_1^2+\bar{\alpha}_2^2=1$. The reduced equilibrium equation for this case can be written as

$$(\lambda_c+\Delta\lambda)\bar{\alpha}_1\varepsilon-\Delta\lambda\xi_1+\tfrac{1}{2}\phi_{122}\xi_2^2+\cdots=0$$
$$(\lambda_c+\Delta\lambda)\bar{\alpha}_2\varepsilon-\Delta\lambda\xi_2+\phi_{122}\xi_1\xi_2+\cdots=0 \tag{70}$$

It has been shown by Koiter (1945) and by Triantafyllidis and Peek (1992) that the worst shape of a geometric imperfection corresponds to the incremental displacements on the bifurcated branch of the perfect structure for which the load drops most rapidly. This is the solution branch given by eqn (66), and corresponds to the two descending bifurcated branches shown in Fig. 5. Thus it is seen that the worst shape of imperfection is given by

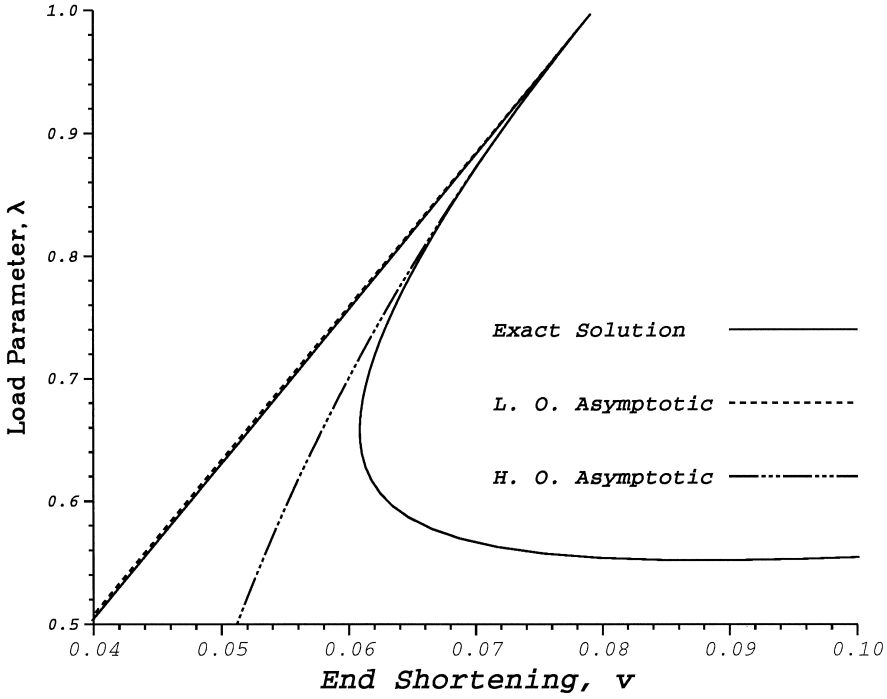

Fig. 6. Relation between load and end-shortening of a cylindrical panel subjected to axial load.

$$\bar{\alpha}_1 = -\sqrt{\tfrac{1}{3}}, \quad \bar{\alpha}_2 = \pm\sqrt{\tfrac{2}{3}} \tag{71}$$

For this case a 'full analysis' is performed by numerically tracking the solutions for the imperfect structure. This requires the analysis to be repeated for a range of values of the imperfection amplitude ε. The results of these analyses are shown in Figs 7 and 8. As can be seen increasing the imperfection amplitude causes the local maximum of the equilibrium path to drop significantly below the bifurcation load of the perfect structure. For instance, one may note that for the imperfection amplitude of 0.2 the limit point is about 56% of the bifurcation load. Figure 7 clearly illustrates the shell's sensitivity to imperfections. The limit point loads obtained from each of these analyses are plotted in Fig. 9 as functions of imperfection amplitude under the label 'Full Analysis'.

For the asymmetric bifurcation, the drop in the load carrying capacity of the structure (defined as the difference between the load λ at the bifurcation point and that at the first limit point for the imperfect structure) can be written as (see e.g. Triantafyllidis and Peek, 1992)

$$\frac{\Delta\lambda}{\lambda_c} = 2\left(\frac{-\bar{\lambda}_1}{\lambda_c}\right)\varepsilon^{1/2} + O(\varepsilon) \tag{72}$$

This result can be obtained from only the leading order terms in eqn (70). This relationship (not including any higher order terms) is shown in Fig. 9 as the 'L.O. asymptotic' result. Therein the modes have been normalized in such a way that $\varepsilon = 1$ represents a maximum geometric imperfection amplitude of one shell thickness.

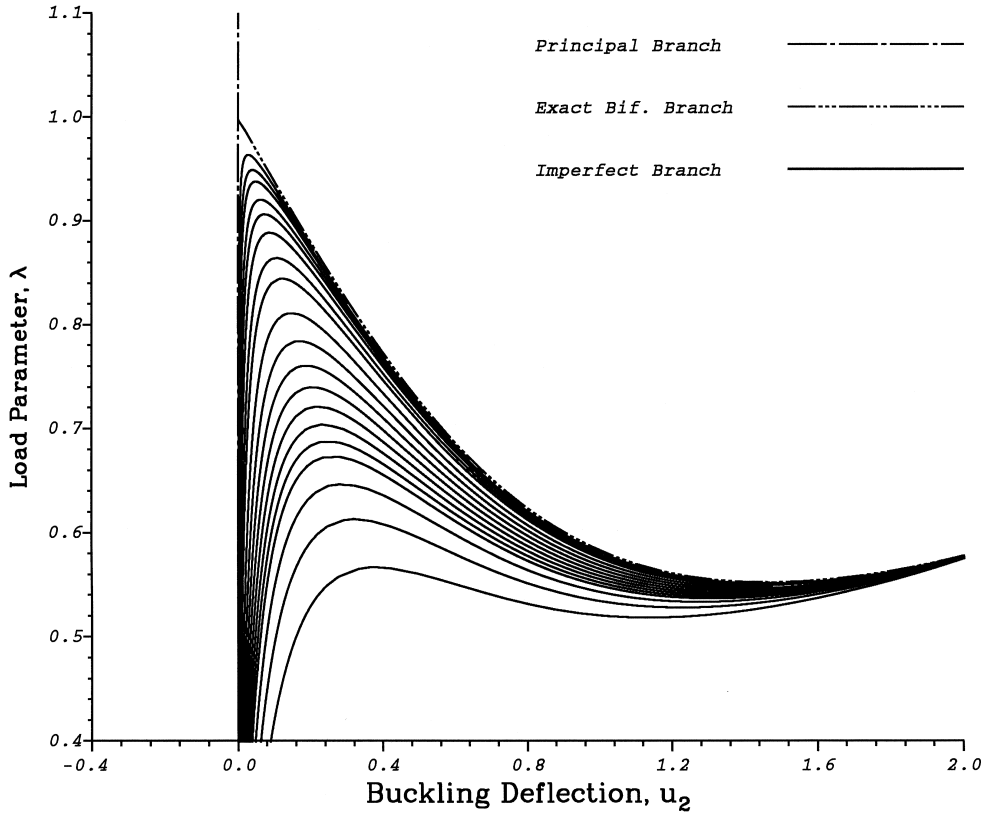

Fig. 7. Equilibrium branches of an imperfect cylindrical panel, the imperfection amplitudes considered are $\varepsilon = 0.001$, 0.002, 0.003, 0.005, 0.007, 0.01, 0.015, 0.02, 0.03, 0.04, 0.05, 0.06, 0.07, 0.08, 0.09, 0.1, 0.12, 0.15, and 0.2.

Including also the term of order $\varepsilon\Delta\lambda$ yields the following improved solution for the load at the limit point (see e.g. Koiter, 1945; Kheyrkhahan, 1995)

$$\frac{\Delta\lambda}{\lambda_c} = \frac{2\bar{\lambda}_1}{\lambda_c}\left[-\varepsilon + \sqrt{\varepsilon^2 - \lambda_c\varepsilon/\bar{\lambda}_1}\right] \tag{73}$$

which is shown in Fig. 9 as the 'Improved Asymptotic' result.

Further improvements in the asymptotic solution can be obtained if one includes also the $\phi_{ijkl}\xi_j\xi_k\xi_l$ terms in eqn (70). In this case one needs to solve the system numerically. It can be shown that for this problem with linear prebuckling solution, this yields a higher order accurate solution, which is therefore shown in Fig. 9 under the label 'H.O. Asymptotics'.

The results in Fig. 9 indicate that all asymptotic calculations predict the drop in the load-carrying capacity with an accuracy better than 10% (of the load drop) for imperfection amplitudes up to $\varepsilon = 0.1$ (i.e. one tenth of the wall thickness). At an imperfection amplitude of $\varepsilon = 0.2$, the accuracy of the improved asymptotic and higher order asymptotic results are still within 10% (on

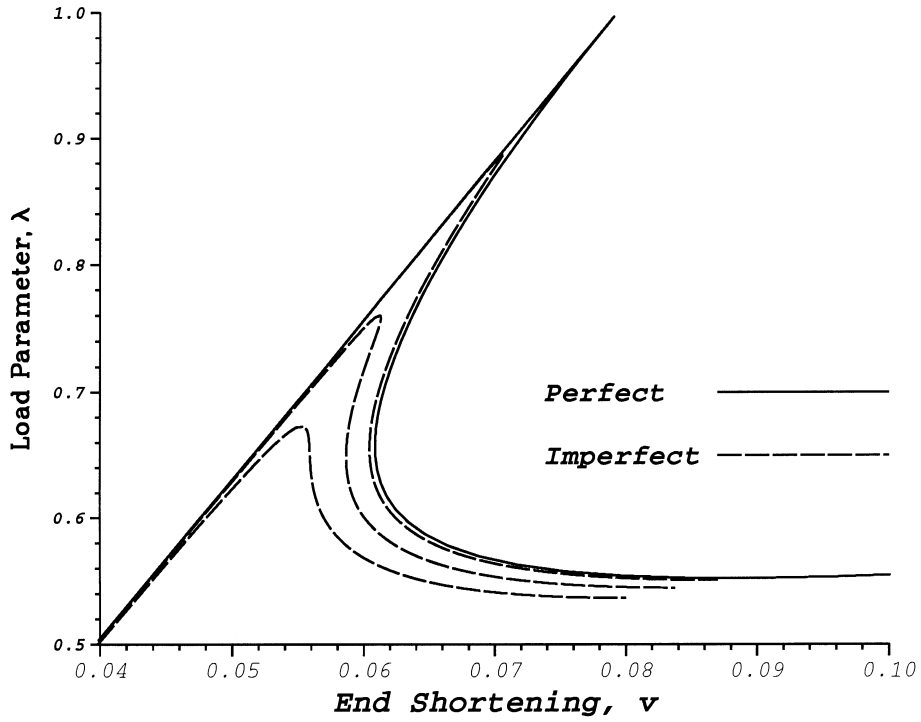

Fig. 8. Equilibrium paths of an imperfect cylindrical panel, the imperfection amplitudes considered are 0.01, 0.05, and 0.1. The fundamental equilibrium path and the bifurcated equilibrium path of the perfect structure are shown in solid lines.

the unconservative side), and for the leading order asymptotic result the accuracy is within 20% (on the conservative side). These errors are not large, compared to what might have been incurred by failing to pick the worst shape of imperfection. For a number of design situations, larger imperfections can occur, and in such circumstances it is still advisable to complement the asymptotic analyses by full analyses of the system. Nevertheless, the asymptotics are still valuable in identifying the worst shapes of imperfection, and gaining an improved overall understanding of the behavior of the structure.

3.5. *Example 2: Cylinder with two closely spaced modes under axial load*

By slightly modifying the dimensions of the cylindrical panel of the preceding example, one obtains a system with two closely-spaced buckling modes. More specifically, the changes made are such that point A in Fig. 2 remains on the Koiter's circle. Thus the axisymetric mode remains at the minimum buckling load of λ_1. However point B (in Fig. 2) moves away from Koiter's circle, and therefore corresponds to a mode with a higher buckling load of $\lambda_2 = 1+\alpha$, say. In this case the reduced equilibrium equations for the perfect system can be written as (see Kheryrkhanan, 1995)

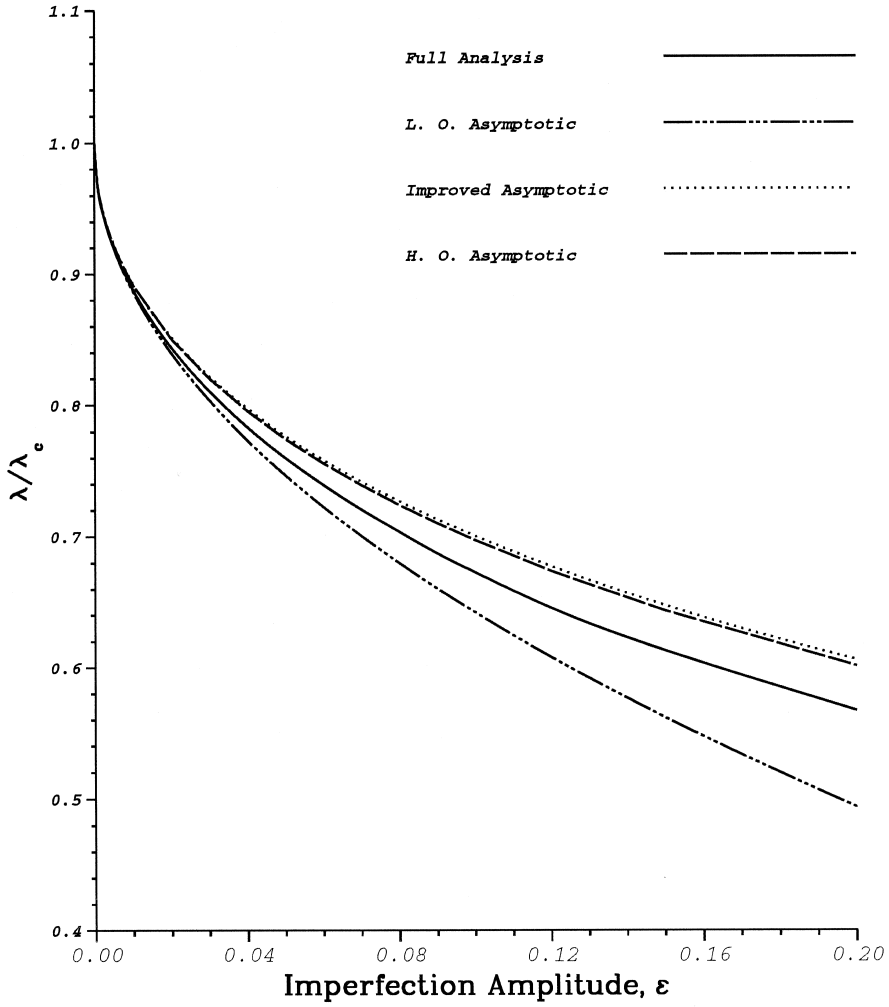

Fig. 9. 'Load drop–imperfection amplitude' diagrams for an imperfect cylindrical panel.

$$(\lambda_1-\lambda)\xi_1+\tfrac{1}{2}\phi\xi_2^2+\cdots=0 \tag{74}$$

$$(\lambda_2-\lambda)\xi_2+\phi\xi_1\xi_2+\cdots=0 \tag{75}$$

where $\lambda_i=\lambda_c+\mu_i$ is the buckling load as calculated from the linearized eigenvalue problem [eqn (6)]. One solution to the above is an axisymmetric case given by

$$\xi_2=0,\quad \lambda=\lambda_1,\quad \text{and}\quad \xi_1 \text{ arbitrary} \tag{76}$$

There are no solutions involving $\xi_1=0$ except the principal branch. If $\xi_2\neq 0$ then from eqn (75) we have

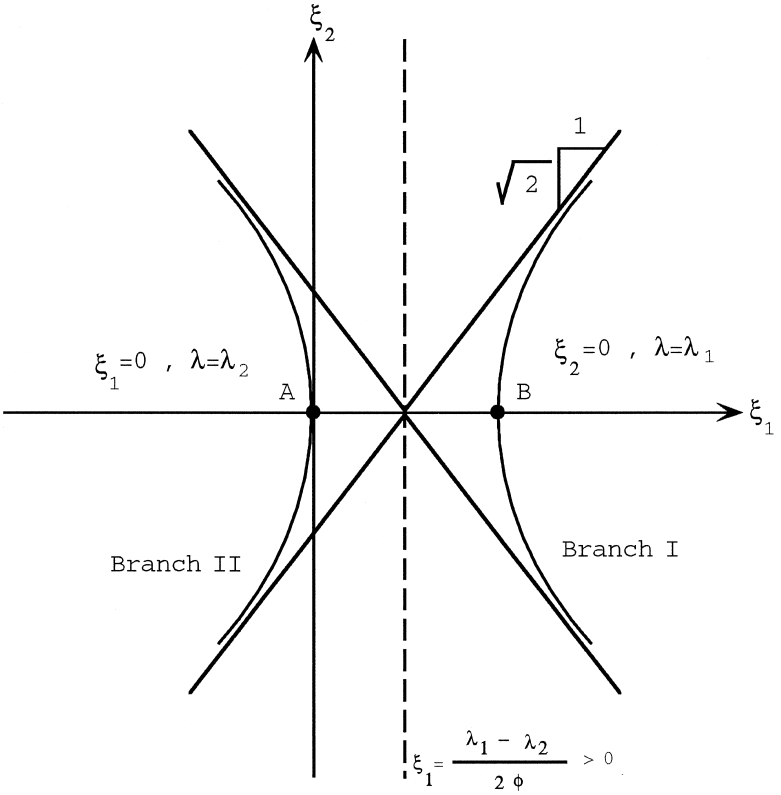

Fig. 10. Schematic figure of the asymptotic solutions to the bifurcated branches of a cylinder with non-coincident modes.

$$\lambda = \lambda_2 + \phi\xi_1 \tag{77}$$

Substitution into (74) results in

$$(\lambda_1 - \lambda_2 - \phi\xi_1)\xi_1 + \tfrac{1}{2}\phi\xi_2^2 = 0 \tag{78}$$

Since $\lambda_1 - \lambda_2$ is small, the ratio of ξ_1 and ξ_2 for very large values is given by

$$\xi_1 \sim \pm\frac{\xi_2}{\sqrt{2}} \tag{79}$$

At the point where $\xi_2 = 0$, the parameter ξ_1 is either zero or is found from $\xi_1 = (\lambda_1 - \lambda_2)/\phi$. Substitution of ξ_1 into (77) gives $\lambda = \lambda_1$. Therefore, this point is on the same solution as (76). A simple change of variables $\{\eta = \xi_1 - [(\lambda_1 - \lambda_2)/2\phi]\}$ and substitution into (78) leads to the hyperbolic relation

$$\left(\frac{\lambda_1 - \lambda_2}{2\phi}\right)^2 - \eta^2 + \frac{1}{2}\xi_2^2 = 0 \tag{80}$$

which is symmetric about $\eta = 0$ and $\xi_2 = 0$. The above equation is shown in Fig. 10. Regarding the sign of $(\lambda_1 - \lambda_2)/\phi$ there are several possibilities. For $[(\lambda_1 - \lambda_2)/\phi] > 0$ one obtains:

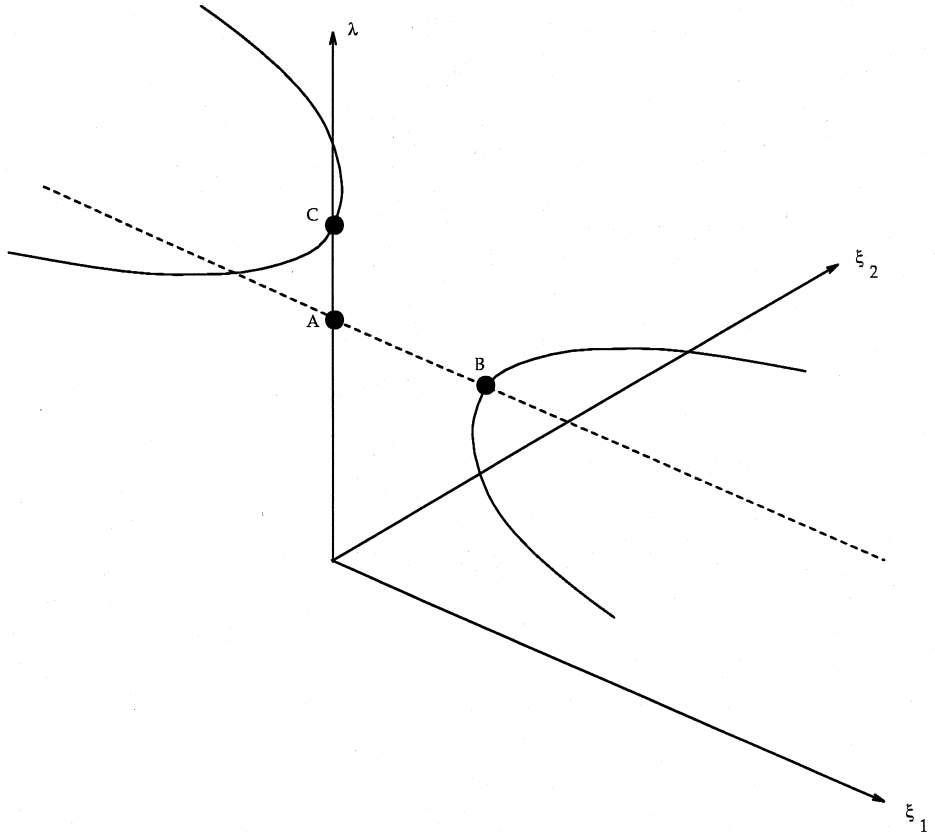

Fig. 11. Schematic figure of the bifurcated branches for a cylinder with non-coincident modes.

$$\text{If } \phi < 0 \quad \text{and} \quad \lambda_1 < \lambda_2 \quad \text{then} \begin{cases} \text{branch (I) descending} \\ \text{branch (II) ascending} \end{cases} \tag{81}$$

$$\text{If } \phi > 0 \quad \text{and} \quad \lambda_1 > \lambda_2 \quad \text{then} \begin{cases} \text{branch (I) ascending} \\ \text{branch (II) descending} \end{cases} \tag{82}$$

In our numerical study ϕ turned out to be negative and $\lambda_1 < \lambda_2$. Therefore, we have $[(\lambda_1 - \lambda_2)/\phi] > 0$ and eqn (81) applies. A schematic drawing of the bifurcated branches in $\xi_i - \lambda$ space is shown in Fig. 11.

The bifurcated solution branches for the perfect structure are shown in Figs 12–14 for mode separations of 5%, 15%, and 25%, respectively. All three bifurcated branches are numerically tracked. Branch switching at the secondary bifurcation point B in Fig. 11 is carefully handled to generate both sides of the descending branch. The asymptotic solutions are shown in Figs 12–14 by solid lines.

In the case of the axisymmetric bifurcated branch (the horizontal dotted lines), the exact and asymptotic solutions coincide. For the rising bifurcated branches, as the two bifurcation points

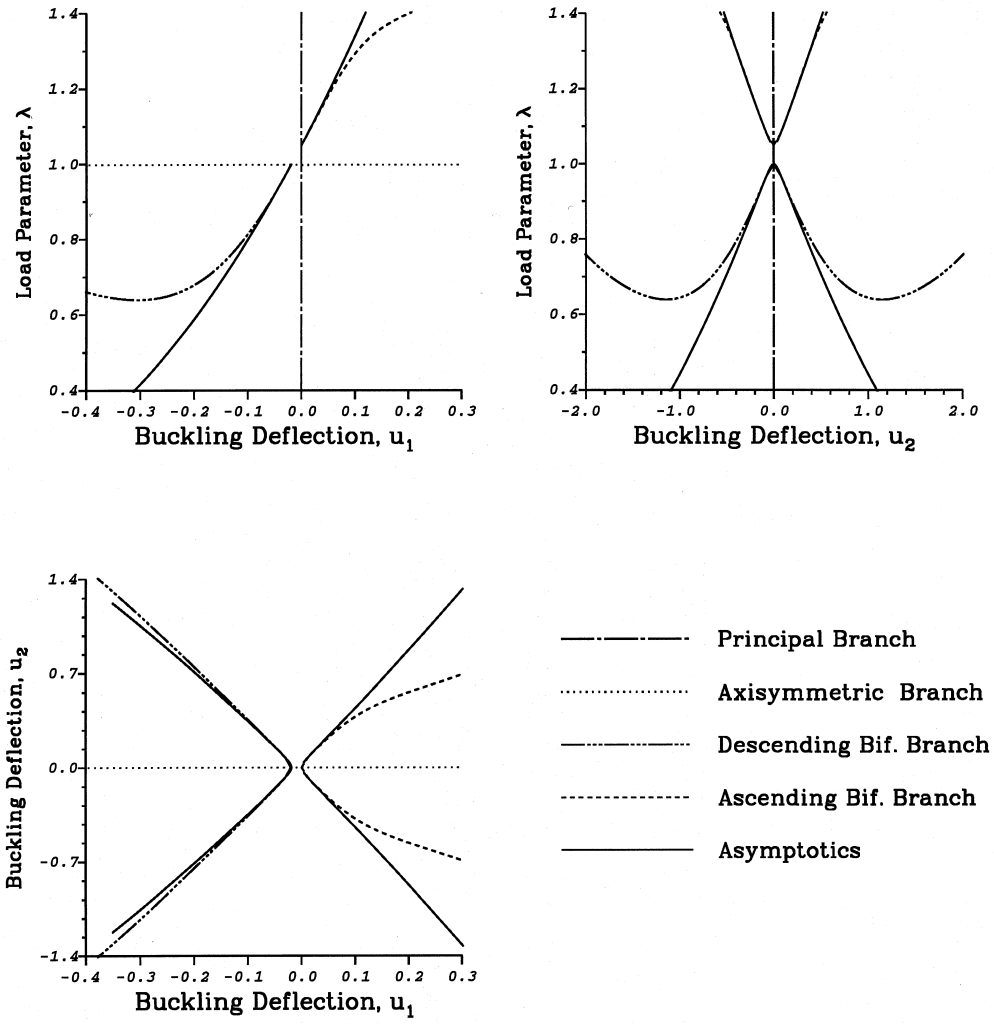

Fig. 12. Bifurcated branches for a cylinder with non-coincident modes, the two bifurcation points are 5% apart.

are moved further apart, the accuracy is not greatly affected. In the case of the descending branches (which are of more interest) the exact solutions and asymptotics agree up to 20% load drop, when the bifurcation points are 5% apart. However, when the two modes are 15% apart the agreement lasts up to 15% load drop. As the modes are moved further apart to 25%, the asymptotics match the exact solutions up to 10% load drop.

This example shows that despite up to 25% mode separation the asymptotics still provide a reasonable approximation to the exact solution in the vicinity of the bifurcation points. Certainly the asymptotics allow one to identify the most critical one of the branches, which in this case is a secondary bifurcated branch. This illustrates how the asymptotics and the full analysis can be used to complement each other, by first identifying the most critical branch with the asymptotics, and

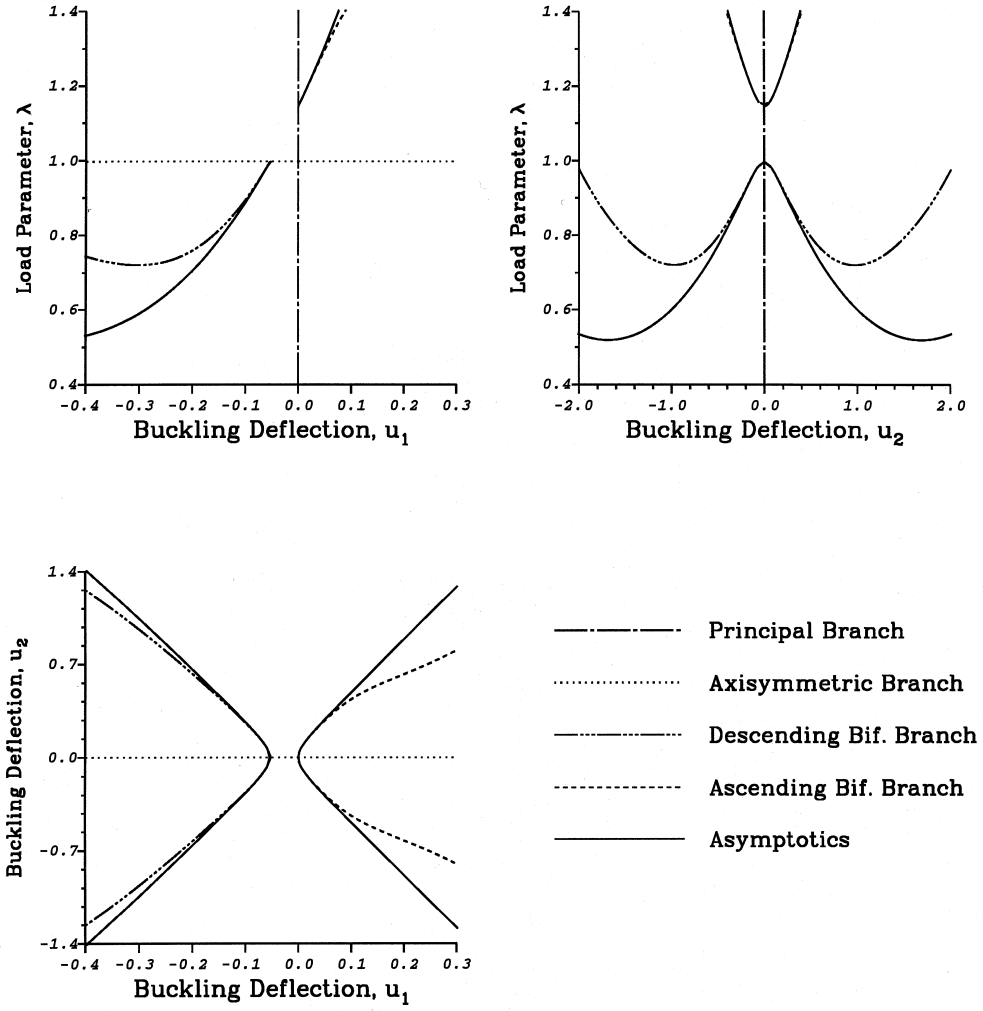

Fig. 13. Bifurcated branches for a cylinder with non-coincident modes, the two bifurcation points are 15% apart.

then using the full solution to track it, in order to obtain more accurate results further away from the bifurcation point.

3.6. *Example 3: Spherical cap subjected to uniform external pressure*

Whereas the previous two examples covered a small number of coincident or non-coincident modes with linear prebuckling behavior, this example has two additional features: nonlinear prebuckling behavior, and a large number of potentially interacting modes. For this purpose, a spherical cap that is fully fixed all around the edge is considered. The radius to thickness ratio is 1000, and the meridional angle from the apex to the lower edge is 20°. Normally for the finite element analysis of shells, it is sufficient for the elements to be small compared to typical dimensions

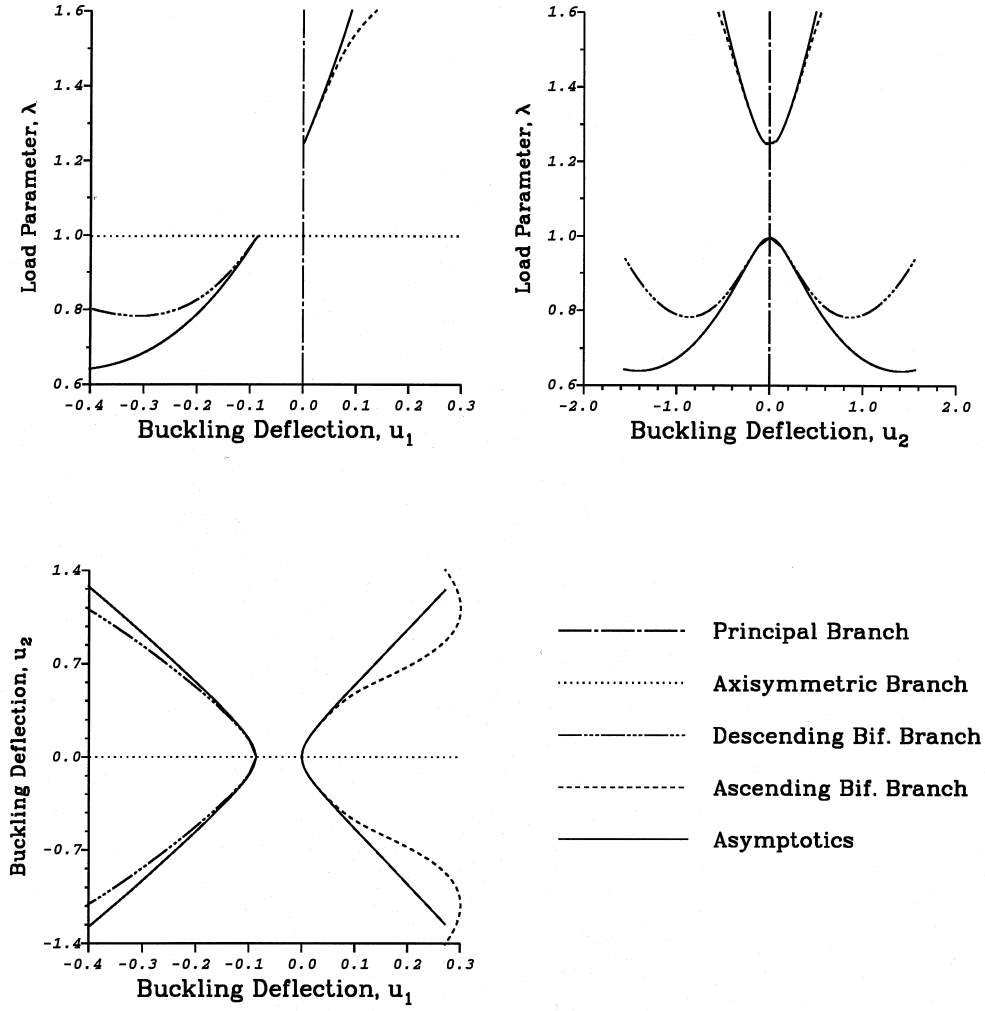

Fig. 14. Bifurcated branches for a cylinder with non-coincident modes, the two bifurcation points are 25% apart.

of the shell, except perhaps in certain boundary layer regions where stresses vary rapidly and some mesh refinement is needed in order to properly resolve these variations. However if the problem involves buckling, it is also necessary for the element size to be small compared to typical buckling wavelengths. The mesh used for this purpose is shown in Fig. 15. It involves 426 nine-node shell elements, 2046 nodal points, and 10,230 degrees of freedom. In view of computing limitations and the large number of solutions that needed to be computed in order to provide the results reported here, only half the shell is modeled, using symmetry boundary conditions. This means that only solutions which are symmetric about a plane through the axis of axisymmetry are considered, even though solutions that do not possess this symmetry are also conceivable.

In order to visualize the bifurcated solutions, it is useful to define buckling displacements as the Discrete Fourier Transform of the transverse displacement at evenly spaced nodes around the

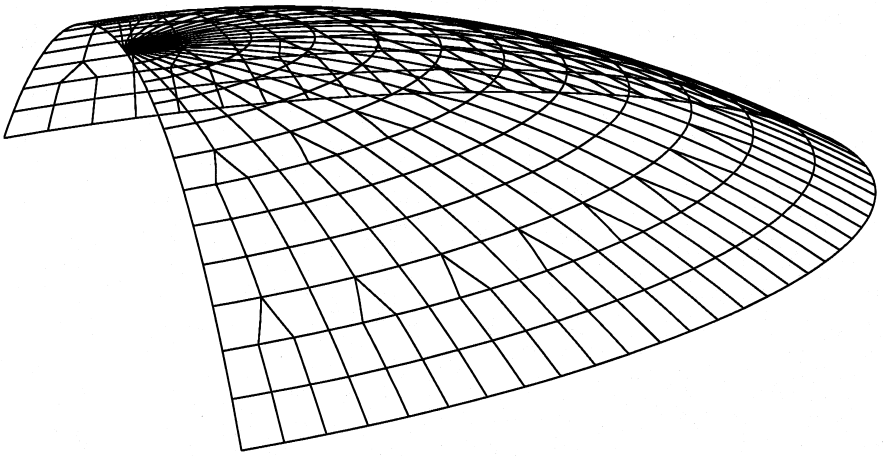

Fig. 15. The finite element mesh used to model the spherical cap.

circumference. If the transverse displacements are denoted by $w_0, w_1, w_2, \ldots, w_N$ for points covering half the circumference (beginning with w_0 on the plane of symmetry, and ending with w_N on the diametrically opposite end of the plane of symmetry), then the buckling displacement can be written as

$$\hat{u}_k = \frac{1}{2N} \sum_{j=-N+1}^{N} w_j \cos\left(\frac{\pi k j}{N}\right), \quad w_{-j} = w_j \tag{83}$$

For the mesh considered the displacements w_j are taken to be those on a circle of nodes at an angle of 16.6° from the apex, for which $N = 108$. The use of these buckling displacements makes it easier to interpret the results, since (except for $k = 0$) the buckling displacements $\hat{u}_k$ are all zero for the principal solution. Furthermore these buckling displacements allow any periodicity of the solution, as well as symmetry-breaking secondary bifurcations to be readily identified.

Results for the bifurcated branches of the perfect structure are shown in Figs 16 and 17. Therein dashed lines are derived from the asymptotics, whereas solid lines correspond to 'exact' results computed by numerically tracking the bifurcated branches. Also solid black dots (of circular shape) identify secondary bifurcations located by the full analysis (by means of a change in the number of negative eigenvalues of the tangent stiffness matrix), whereas hollow dots indicate secondary bifurcations identified by the asymptotics. More specifically, the results for the perfect system were calculated as follows:

(i) The principal solution is calculated by solving the full system up to a point close to the first bifurcation. This point is then used as the reference point, the linearized eigenvalue problem [of eqn (6)] is solved, and the postbuckling coefficients ϕ_{ijk} and ϕ_{ijkl} are calculated. In this case sixteen buckling modes are considered. The corresponding buckling loads and circumferential wavenumbers are shown in Table 1, and the mode shapes are shown in Figs 18–21.

(ii) Since there is some separation of the modes, bifurcated branches emanate from the principal solution at each of the bifurcation loads and in the direction of the corresponding buckling

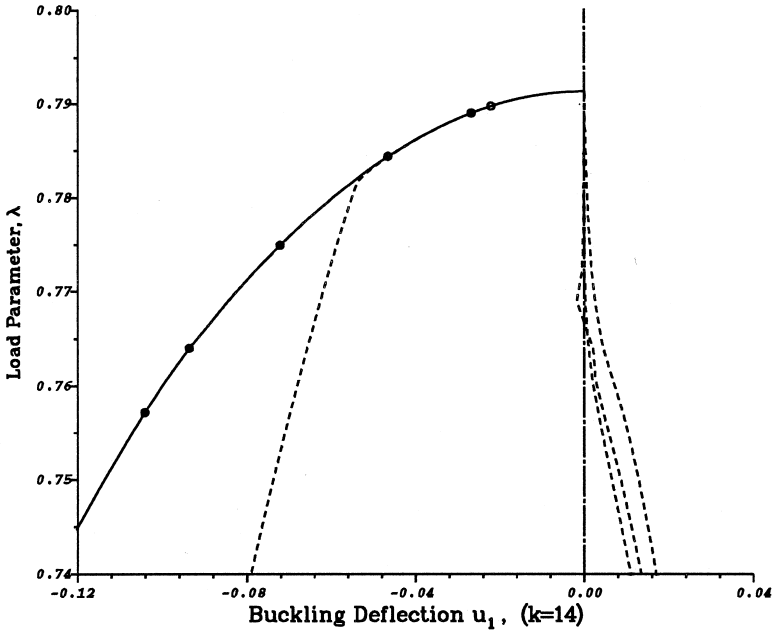

(a) The first mode

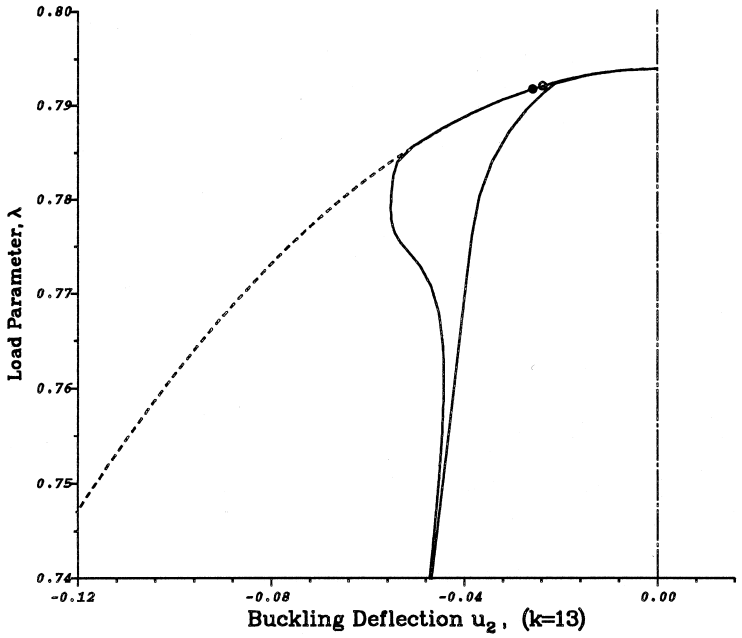

(b) The second mode

Fig. 16. Bifurcated branches for the spherical cap. Solid lines represent the exact solutions and dashed lines represent the asymptotics.

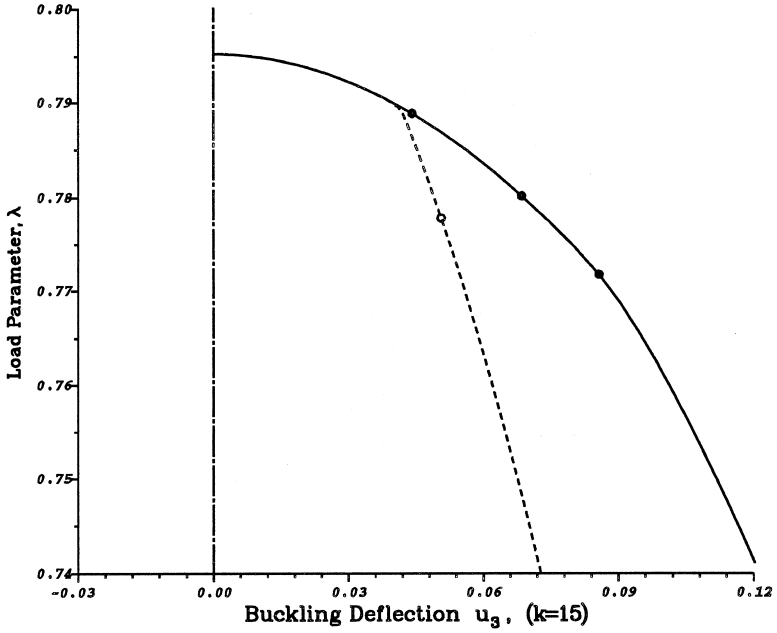

(a) The third mode

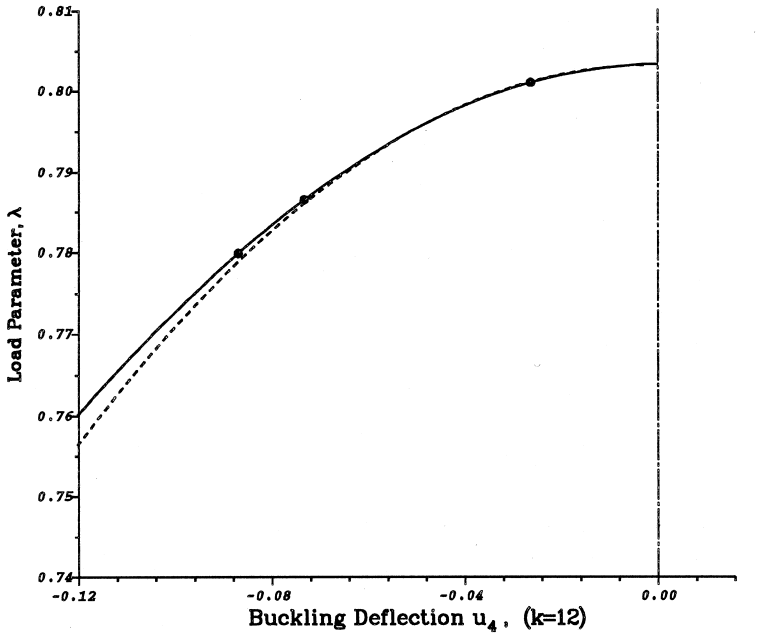

(b) The fourth mode

Fig. 17. Bifurcated branches for the spherical cap, continued. Solid lines represent the exact solutions and dashed lines represent the asymptotics.

Table 1
The buckling loads and their wave numbers for the spherical cap subjected to uniform pressure

Buckling mode	Wave number	Buckling load
1	14	0.79136
2	13	0.79397
3	15	0.79525
4	12	0.80323
5	16	0.80514
6	11	0.81917
7	17	0.82042
8	10	0.84124
9	18	0.84342
10	19	0.86566
11	9	0.86959
12	20	0.89430
13	8	0.90538
14	21	0.92675
15	9	0.93206
16	8	0.93486

mode. These bifurcated branches were tracked numerically for modes 1 to 4 and are denoted by solid lines in Figs 16a, b and 17a, b, respectively.

(iii) In a similar way as for the full system, the reduced equilibrium equations are solved including all sixteen modes. This is achieved with the same numerical procedure for tracking the bifurcated branches as is used for the full system, except that in this case there are only 16 equations with 16 unknowns. The ϕ_{ijk} terms as well as the ϕ_{ijkl} terms are included in the reduced equilibrium equations. Once the modal displacements ξ_i are obtained, the corresponding buckling displacements denoted in Figs 16 and 17 by dashed lines are computed with the aid of eqn (83).

Examine first the bifurcated branch corresponding to mode 1 (circumferential wavenumber $k = 14$) shown in Fig. 16a. Initially the exact solution (solid line) and asymptotic solution (dashed line) coincide, so that it is impossible to distinguish them. The asymptotics also reproduce the location of the first secondary bifurcation fairly accurately, as can be seen from two nearby dots, one solid and the other hollow. This first secondary bifurcated branch was not tracked. Continuing instead on the primary bifurcated branch, a second secondary bifurcation point is located by the full analysis, but the asymptotic solution veers off at approximately the same point. This suggests that due to some inadvertent imperfection the asymptotic solution has switched to a secondary bifurcated branch.

Unintended imperfections can also be observed by examining the buckling displacements for circumferential wavenumbers $k = 8$, 10, and 12, shown in Fig. 16a by dashed lines close to the principal branch. These are seen to be small, but they should be zero. Indeed, the bifurcated branch

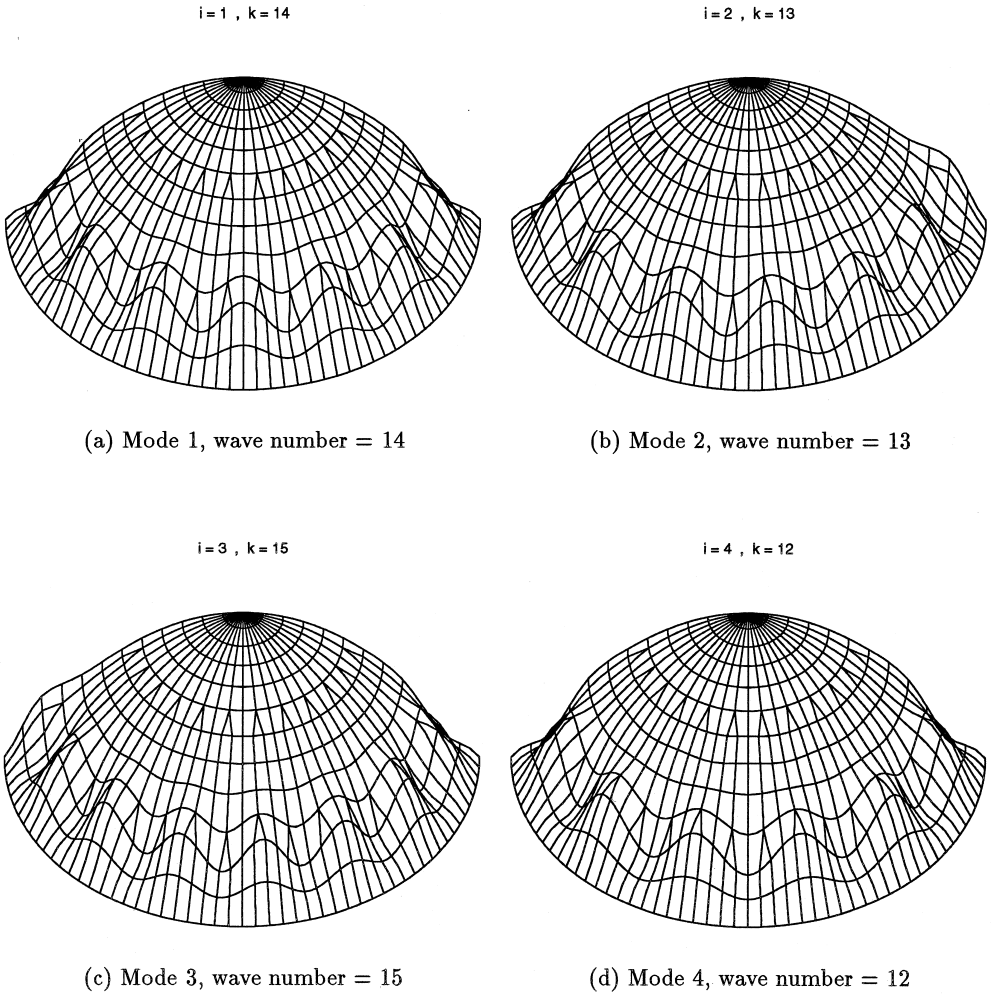

(a) Mode 1, wave number = 14 (b) Mode 2, wave number = 13

(c) Mode 3, wave number = 15 (d) Mode 4, wave number = 12

Fig. 18. Buckling modes of a spherical shell subjected to uniform pressure.

under investigation should be periodic in the circumferential direction with $k = 14$ repetitions of the same solutions around the circumference. This means that only the buckling displacements for wavenumbers $k = 0, 14, 28, 42, \ldots$ can be nonzero, except if a symmetry-breaking secondary bifurcation occurs (see e.g. Wohlever, 1993; Healy, 1988). Therefore, the observed deviations from zero for buckling displacements corresponding to $k = 8$, 10, and 12 waves are due to imperfections. Such imperfections arise because of the finite element discretization.

According to the symmetry group terminology used by Healy (1988) and Wohlever (1993) the symmetries of the spherical cap are those of a continuous dihedral group denoted by D_∞. Any amount of rotation about the axis of axisymmetry, or a reflection about a plane through this axis does not alter the structure. However for the discretization used the mesh is periodic with $k = 12$ repetitions of the same mesh pattern around the circumference. In addition each unit cell is

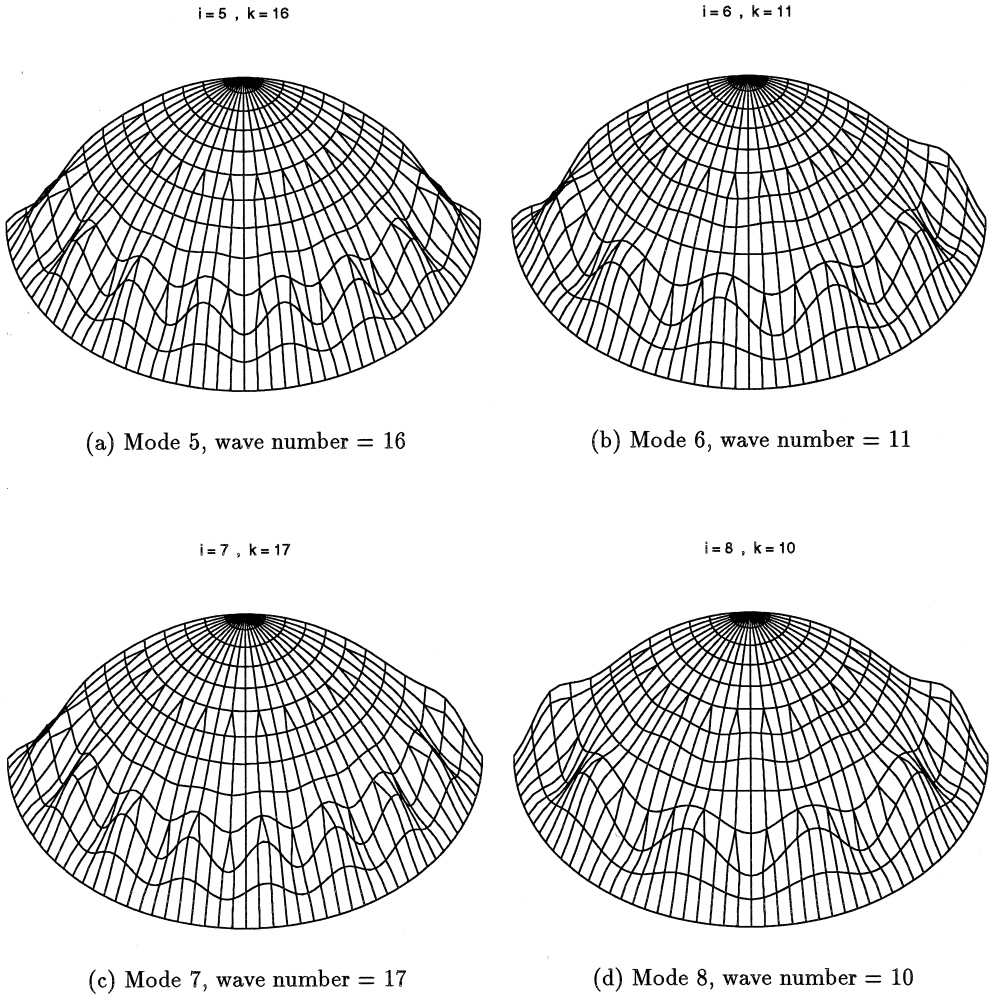

(a) Mode 5, wave number = 16

(b) Mode 6, wave number = 11

(c) Mode 7, wave number = 17

(d) Mode 8, wave number = 10

Fig. 19. Buckling modes of a spherical shell, continued.

symmetric. This corresponds to the dihedral symmetry group denoted by D_{12}. Therefore, except for the mode with circumferential wavenumber $k = 12$, the discretized structure is not a perfect one. This explains the non-zero buckling displacements for $k = 8$, 10, and 12, and also the tendency for the numerical tracking of the bifurcated branches to veer off onto secondary bifurcated branches. Indeed the veering of the bifurcated branches is also observed for the bifurcated branches corresponding to modes 2 and 3 (see Figs 16b and 17a, respectively). However for mode 4 with $k = 12$ (Fig. 17b) there is no veering of the bifurcated branches, as expected, because in regard to this bifurcated branch the discretized structure is perfect, and the only inadvertent imperfections that could arise are due to numerical truncation errors, which in this case (using double precision computer arithmetic with an accuracy of about 16 decimal digits) are significantly smaller than the discretization error.

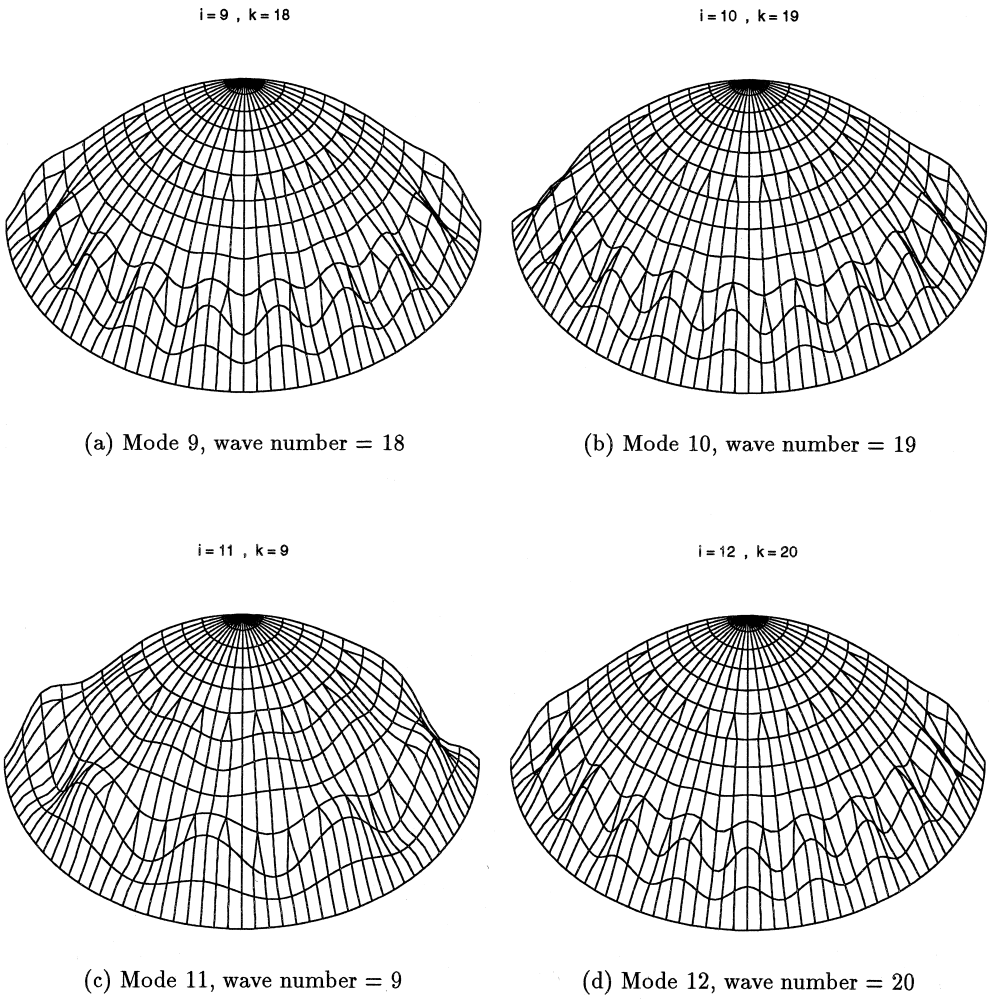

(a) Mode 9, wave number = 18 (b) Mode 10, wave number = 19

(c) Mode 11, wave number = 9 (d) Mode 12, wave number = 20

Fig. 20. Buckling modes of a spherical shell, continued.

Of all the solutions for the perfect spherical cap shown in Figs 16 and 17 it appears that the only significant differences between the asymptotic and exact solutions arise when these represent different solution branches. This means that the accuracy of the asymptotics still is very good in the range examined. However an extremely complicated picture emerges for the bifurcation diagram of this structure. Even though the asymptotics make it possible to compute the solutions more rapidly, there are just too many solution branches to be computed if one wants to obtain the full bifurcation diagram (which includes secondary branches, tertiary branches, etc.). Indeed Figs 16 and 17 provide only a tiny glimpse of the bifurcation diagram for this structure.

If obtaining a full bifurcation diagram for the structure considered is not feasible, there are two other possibilities: one of them is to employ dynamic analysis methods whereby one abandons any attempt to obtain static equilibrium solutions on the bifurcated branches, and instead models the

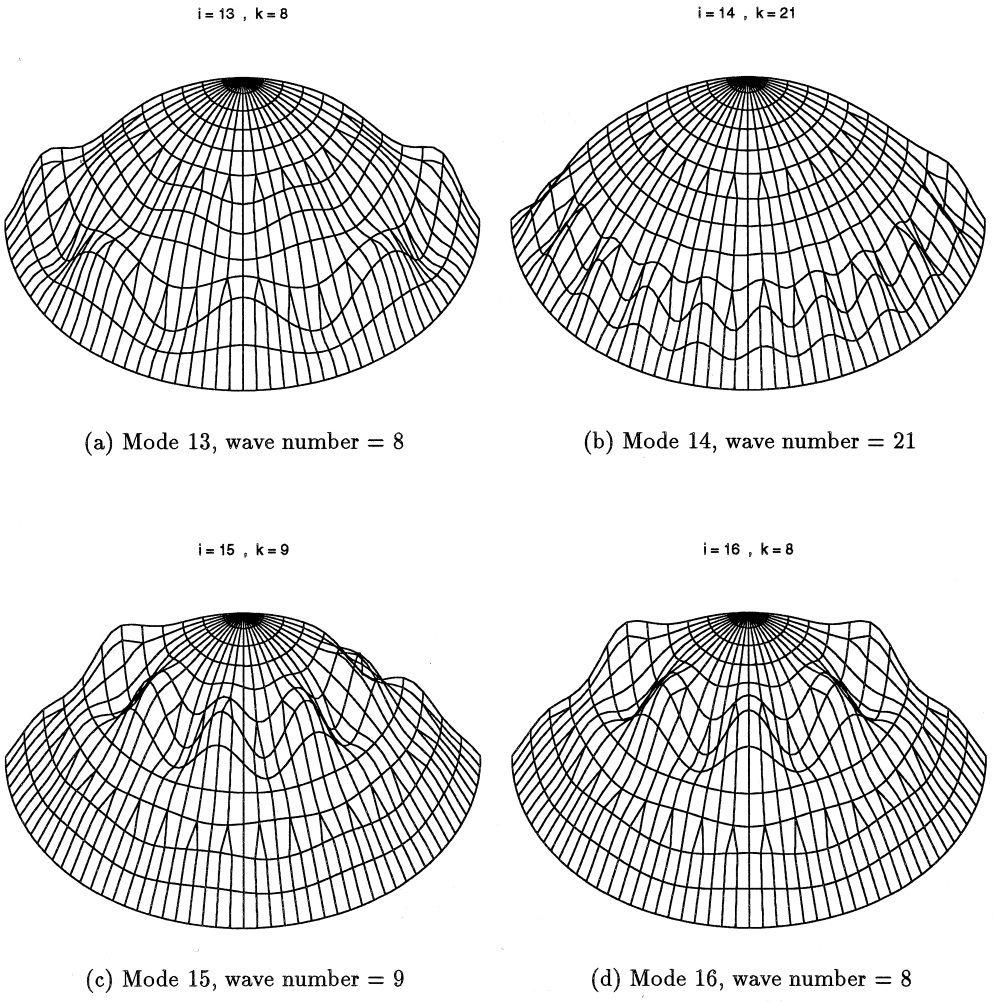

(a) Mode 13, wave number = 8

(b) Mode 14, wave number = 21

(c) Mode 15, wave number = 9

(d) Mode 16, wave number = 8

Fig. 21. Buckling modes of a spherical shell, continued.

dynamic behavior of the system after loss of stability. The other approach is to include a geometric imperfection, and examine its effect on the load carrying capacity of the structure. For a design problem, where one wants to avoid loss of stability, rather than understand what happens if loss of stability does occur, this imperfection based approach is still an appealing one. However, in lieu of a complete bifurcation diagram, one lacks the information as to what the worst shape of imperfection might be. Therefore it is particularly important to perform the analysis for various shapes of imperfections so that one can cover the worst situation that might arise in the actual structure. Again it is here that the asymptotic methods can help, by reducing the computational effort required for every imperfection considered by several orders of magnitude.

In order to investigate the possibilities of the asymptotics in predicting imperfection sensitivity we introduce random geometric imperfections into the spherical cap. For comparison, the equi-

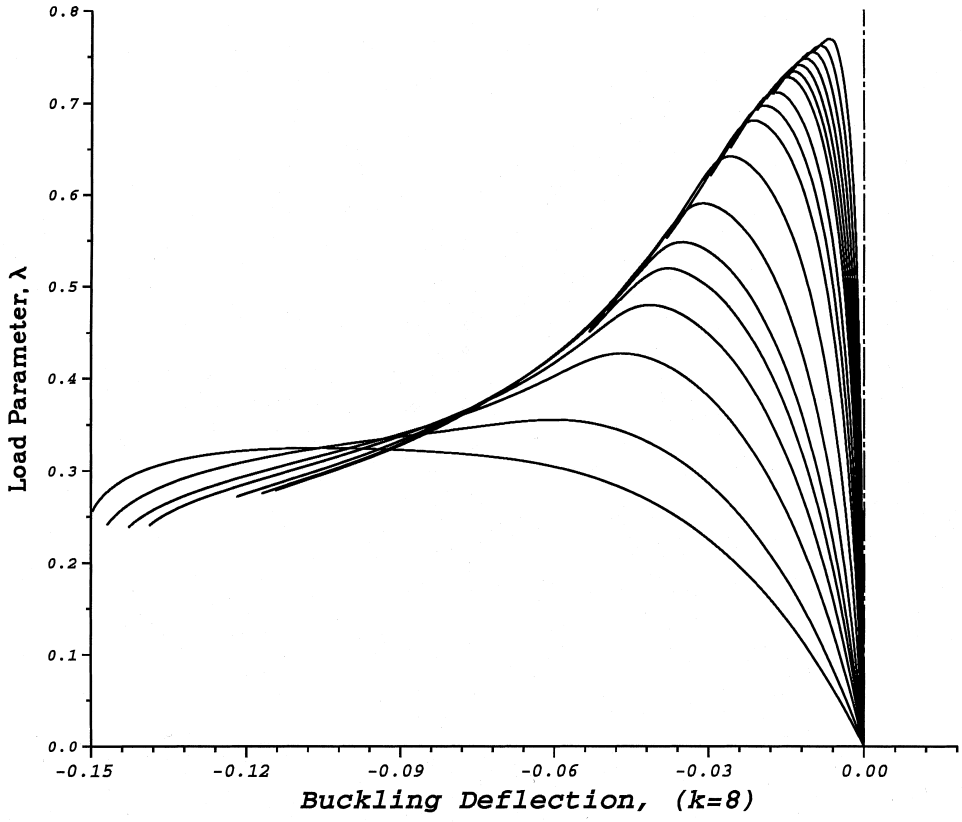

Fig. 22. Equilibrium paths of a spherical cap with random imperfections, the imperfection amplitudes considered are $\varepsilon = 0.06, 0.08, 0.1, 0.12, 0.14, 0.16, 0.18, 0.23, 0.28, 0.34, 0.5, 0.75, 1.0, 1.2, 1.5, 2.0, 3.0$, and 4.0.

librium paths for several imperfection amplitudes are tracked numerically (Fig. 22). The first local maximum (limit point) of each curve in Fig. 22 provides one point on the load drop-imperfection amplitude diagram. This 'exact' solution is shown with a solid line in Fig. 23.

The relation between the imperfection amplitude and the drop in the load carrying capacity is generated by the LSK method with little effort. One simply solves the reduced equilibrium eqns (25), by numerically tracking the equilibrium branch for the imperfect system starting at low values of the load parameter λ where a unique solution can readily be identified. This process is repeated for as many imperfection amplitudes as are necessary to generate a smooth curve. The results are shown in Fig. 23 for different truncations of the Taylor series for the reduced equilibrium equations. Specifically for the curve labeled ϕ_{ijk}, the terms corresponding to the postbuckling coefficients $\phi_{i\varepsilon}$, ϕ_{ij}, $\phi_{ij\lambda}$, and ϕ_{ijk} are included. For the curve labeled $\phi_{i\varepsilon\lambda}$, the $\phi_{i\varepsilon\lambda}$ term is included as well by approximating it by $\phi_{i\varepsilon\lambda} \approx \phi_{i\varepsilon}/\lambda_c$, a relationship that is strictly valid only for linear prebuckling, but is also used here as an approximation. Finally for the curve labeled 'ϕ_{ijkl}', the ϕ_{ijkl} terms are included as well as all of the above. As can be seen in Fig. 23, the LSK method can provide an accuracy of better than 10% up to imperfections that are two and a half times the shell thickness.

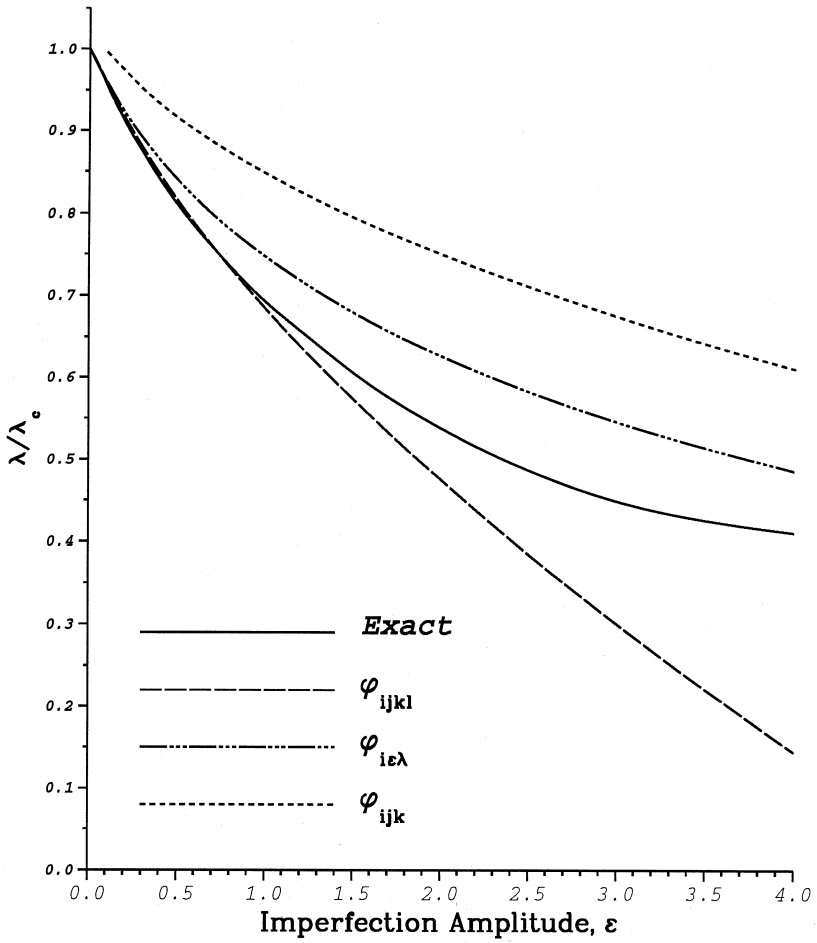

Fig. 23. 'Load drop–imperfection amplitude' diagrams for a spherical cap with random imperfections.

Instead of using a random imperfection, one can also pick imperfections according to the mode shapes that are expected to interact most strongly. This requires certain relationships between the wavenumbers of the interacting modes. For this spherical cap the lowest wavenumber among the 16 buckling modes calculated is $k = 8$, which belongs to both modes 13 and 16 (Table 1). Mode 5 has the wavenumber of 16 which is twice the wavenumber of mode 13. Peek (1995) showed that if the wavenumbers corresponding to the modes i, j and k in ϕ_{ijk} are m_i, m_j, and m_k, then one can only obtain a nonzero ϕ_{ijk} if $m_i \pm m_j \pm m_k = 0$. This condition is satisfied for modes 5 and 13. Thus, we expect that the third order postbuckling coefficient $\phi_{5,13,13}$ be nonzero as indeed it is.

The imperfection is chosen to correspond to the incremental displacements that would occur on the most steeply descending bifurcated branch involving the interaction of modes 5 and 13, if modes 5 and 13 were fully coincident. This leads to an imperfection shape given by

$$\bar{u} = \varepsilon\left(\sqrt{\tfrac{1}{3}}\,\overset{5}{\tilde{u}} + \sqrt{\tfrac{2}{3}}\,\overset{13}{\tilde{u}}\right) \tag{84}$$

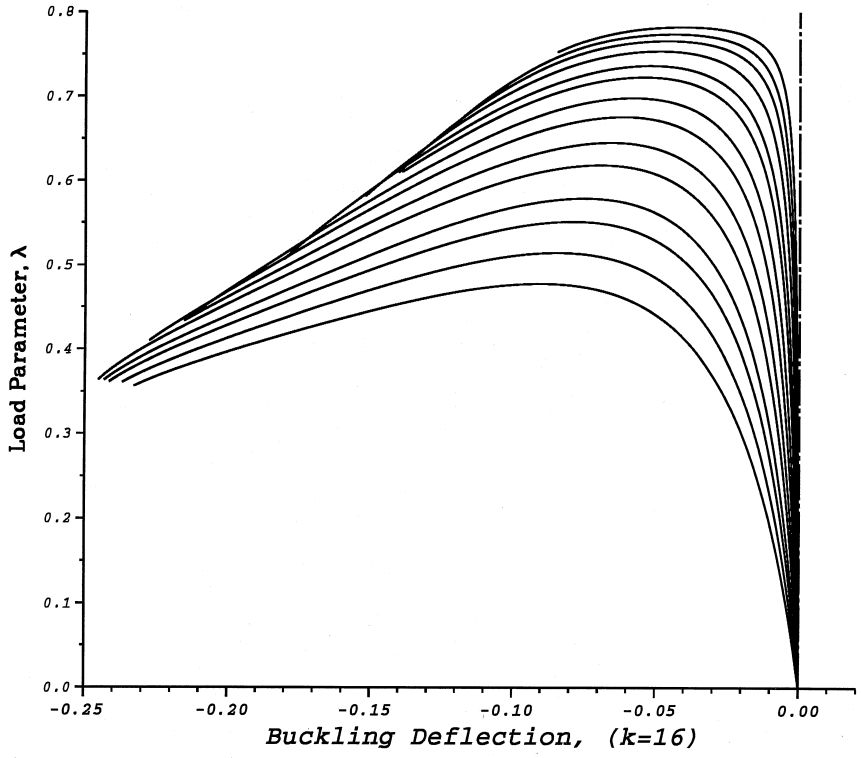

Fig. 24. Equilibrium paths of a spherical cap with an imperfection in the form of a linear combination of modes 5 and 13 (wave numbers 16 and 8, respectively). The imperfection amplitudes considered are: $\varepsilon = 0.1, 0.15, 0.2, 0.28, 0.4, 0.5, 0.7, 0.9, 1.2, 1.5, 2.0, 2.4, 3.0, 3.7$. Buckling deflection shown is for wavenumber 16.

The same imperfection sensitivity analyses performed for the random imperfection, are also performed for this imperfection shape, with the results shown in Figs 24–26. The equilibrium branches obtained from the analysis of the full system for various amplitudes of imperfection are shown in Figs 24 and 25 for buckling displacements corresponding to modes 5 and 13, respectively. As expected, only the buckling displacements corresponding to these wavenumbers were found to be nonzero.

The results in Fig. 26 show excellent agreement with the exact solution when the third and fourth order postbuckling coefficients are included.

4. Conclusions

After having extended the Lyapunov–Schmidt–Koiter decomposition and asymptotic expansion technique to include nonlinear prebuckling behavior as well as multiple not necessarily coincident modes (Peek and Kheyrkhahan, 1993), this paper focuses on the application of this framework to general shells modeled by the finite element method. For this purpose a conventional displacement-based nonlinear shell element formulation (with four to nine nodes and selective reduced inte-

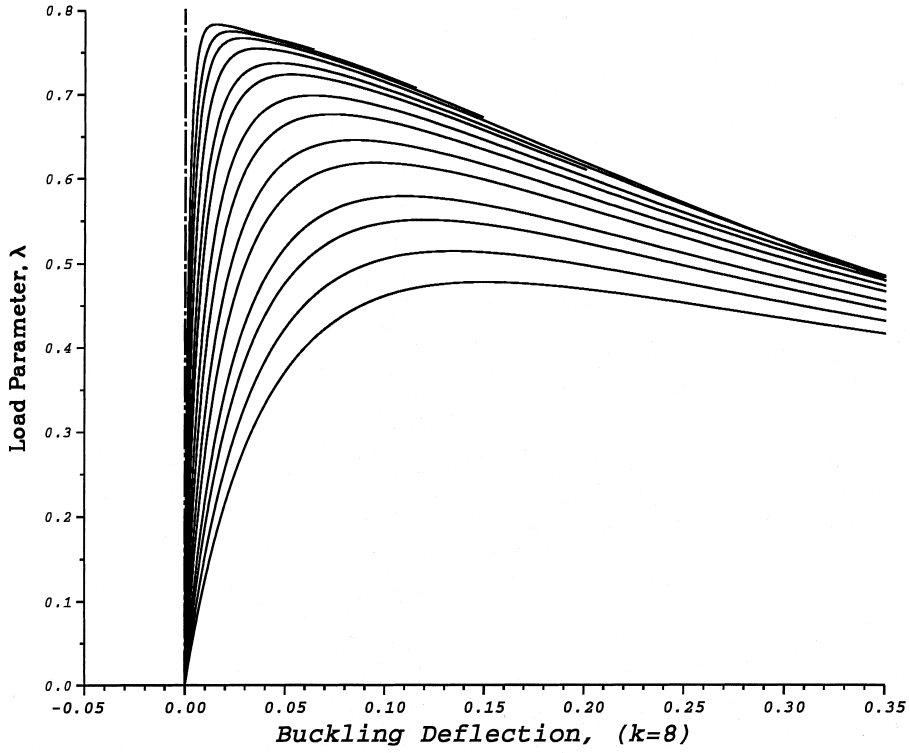

Fig. 25. Equilibrium paths of a spherical cap with an imperfection in the form of a linear combination of modes 5 and 13 (wave numbers 16 and 8, respectively). The imperfection amplitudes considered are: $\varepsilon = 0.1, 0.15, 0.2, 0.28, 0.4, 0.5, 0.7, 0.9, 1.2, 1.5, 2.0, 2.4, 3.0, 3.7$. Buckling deflection shown is for wavenumber 8.

gration) is developed with capabilities to evaluate (analytically) the derivatives of the potential energy with respect to the nodal displacements up to the fourth order, as well as the derivatives with respect to the nodal coordinates needed for the imperfection sensitivity analysis. The resulting 'LSK shell element' is integrated into a general purpose nonlinear finite element program, and used for examples covering nonlinear prebuckling behavior as well as multiple potentially interacting modes (coincident or not).

The advantage of the method is that it allows the bifurcation diagram for the structure (i.e. all solutions in the neighborhood of a bifurcation point) to be investigated with a reduced set of equilibrium equations, with one degree of freedom for each potentially interacting mode. Thus the finite element analyst may view the LSK approach as a nonlinear static condensation, in which the reduced set of equilibrium equations are in the form of a Taylor series expansion. Including only the leading order term in the series can already provide significant insight into the behavior of the system. Comparison of the asymptotic results from the truncated Taylor series for the reduced equilibrium equations with 'exact' results reveals that including certain higher order terms significantly improves the accuracy of the asymptotic results. The asymptotic predictions were found to have good accuracy within about 20% of the bifurcation load, and for mode separations up to 25%.

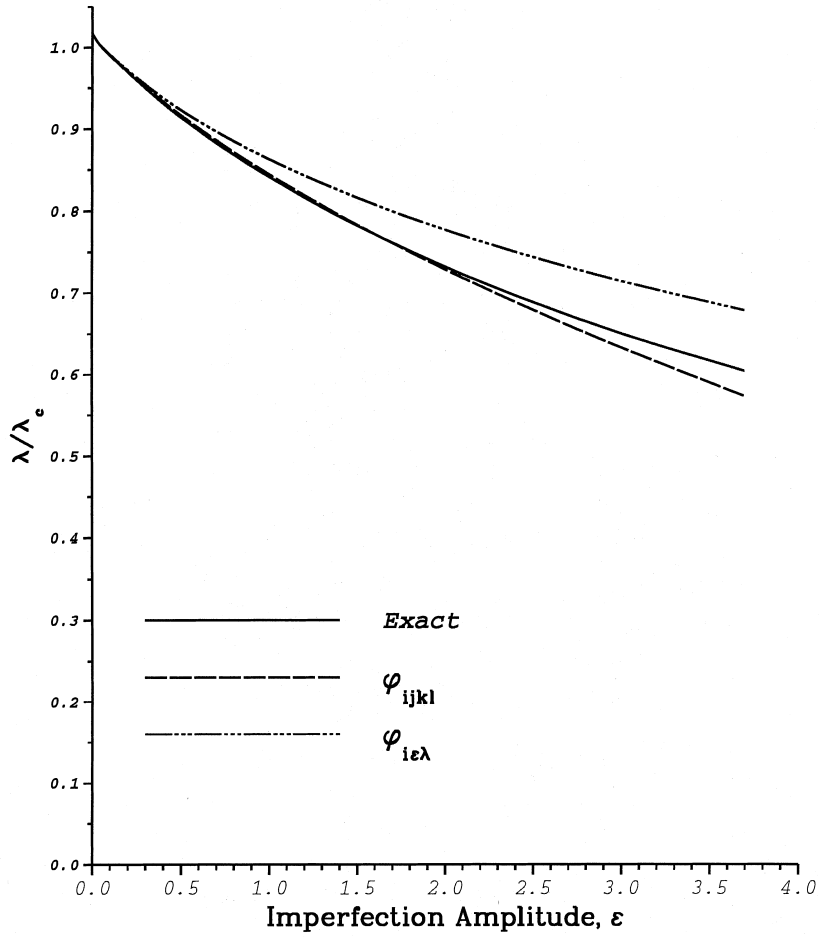

Fig. 26. 'Load drop–imperfection amplitude' diagrams of a spherical cap. The imperfection considered is a linear combination of modes 5 and 13.

For many applications the number of potentially interacting modes becomes quite large. For instance for the spherical cap problem considered here, 16 potentially interacting modes were included in the asymptotic analysis. In this case, the asymptotics were still found to give accurate results, where the 'exact' and asymptotic solutions could be compared for the same solution branch. Thus the range of validity of the asymptotics was not exceeded. However the bifurcation diagram that emerges is so complex, that computing all the bifurcated branches, secondary bifurcated branches, and so on in the vicinity of the primary bifurcation points does not seem currently feasible, even though the asymptotics reduce the computational effort required by several orders of magnitude. More specifically, even with the range of validity of the asymptotics, the bifurcation diagram is too complex and it is not feasible to obtain a full picture of it. In this case it is preferable to use the asymptotics to investigate the imperfection sensitivity of the structure.

The LSK shell element developed also allows the leading order term in the reduced equilibrium

equations to be calculated for an arbitrary geometric imperfection. Therefore, the asymptotics can also be used to calculate the drop in the load carrying capacity of the structure due to imperfections. Here too, the accuracy of the asymptotics is found to be good for imperfections producing drops in the load carrying capacity of up to somewhere between 20–50% depending on the specific example considered. This corresponds to geometric imperfection amplitudes of the order of the shell thickness (more precisely, in case of the cylindrical panel the imperfection amplitudes were up to one fifth of the shell thickness, and in the case of the spherical cap the imperfection amplitudes were as large as two and a half times the shell thickness). Indeed for the cylindrical shell it is observed (by numerically tracking the equilibrium path) that imperfections larger than one fifth the shell thickness do not even produce a limit point (see Fig. 7). In this case, the range of validity of the asymptotics is as good as it can possibly be.

Finally it is worth comparing this methodology for investigating (multiple) bifurcations with the symmetry group approach developed by Healy and Wohlever (1988, 1993). Their approach is not limited to elastic structures, nor is there any question about a potentially limited range of validity of the asymptotics. Also it allows one to avoid computing solution branches that can be obtained by a symmetry operation such as reflection or rotation on some other solution branch. This symmetry group approach does however require the symmetries of the structure to be described before beginning the analysis, so that these symmetries can be incorporated into the analysis methodology. In contrast, when using the asymptotics, the description of the finite element model is no different from that of a conventional finite element analysis. Essentially the symmetry group approach is more reliable than the asymptotics, but it also tends to require more computational effort to track any given equilibrium branch, since even with exploitation of the symmetries, the systems of equations to be solved tend to be larger than the reduced equilibrium equations of the asymptotic approach. Indeed in the symmetry group approach, the computational effort for tracking the bifurcated branches increases, with each symmetry-breaking bifurcation. Therefore, for structures with very complex bifurcation diagrams, such as the spherical cap considered here, obtaining a complete picture of the bifurcation diagram may still not be feasible.

For the case of the imperfect structures, symmetries are broken. So there is less advantage in using the symmetry group approach. Indeed a general random imperfection will break all symmetries. This renders the symmetry group approach not applicable, whereas the asymptotic approach can still be used.

Despite the arguments presented, the asymptotics and symmetry group approach should be regarded as complementary rather than competing methodologies. Indeed one may fail to solve even the reduced equilibrium equations without an understanding of the symmetries of the structure. On the other hand symmetries can also be exploited in conjunction with the asymptotic approach. For instance, for a periodic structure (cyclic symmetry group) the asymptotic reduced equilibrium equations for the whole structure can be derived from a finite element discretization of only one of the unit cells using only the degrees of freedom associated with that unit cell (Peek, 1995).

References

Amazigo, J.C., Budiansky, B., Carrier, G.F., 1970. Asymptotic analysis of the buckling of imperfect columns on nonlinear elastic foundations. Int. J. Solids Structures 6, 1341–1356.

Basar, Y., Ding, Y., 1995. Inter laminar stress analysis of composites: layer-wise shell finite elements including transverse strains. Composites Engineering 5 (5), 485–499.

Basar, Y., Ding, Y., 1996. Finite element analysis of hyper elastic thin shells with large strains. Comp. Mech. 18 (3) 200–214.

Buchter, N., Ramm, E., 1992. Shell theory versus degeneration; a comparison in large rotation finite element analysis. Int. J. Num. Meth. Eng. 34, 39–59.

Buchter, N., Ramm, E., Roehl, D., 1994. Three dimensional extension of nonlinear shell formulation based on the enhanced assumed strain concept. Int. J. Num. Meth. Eng. 37, 2551–2568.

Budiansky, B., 1974. Theory of buckling and postbuckling behavior of elastic structures. Advances in Applied Mechanics 14, 1–65.

Byskov, E., Hutchinson, J.W., 1977. Mode interaction in axially stiffened cylindrical shells. AIAA Journal 15, 941–948.

Carnoy, E., 1980. Postbuckling analysis of elastic structures by the finite element method. Comp. Meth. in Appl. Mech. and Engineering 23, 143–174.

Healy, T.J., 1988. A group theoretic approach to computational bifurcation problems with symmetry. Comp. Meth. in Appl. Mech. and Engineering 67, 257–295.

Hui, D., Du, I.H.Y., 1987. Initial postbuckling behavior of imperfect, antisymmetric crossply cylindrical shells under torsion. J. Appl. Mechanics 54, 174–180.

Hutchinson, J.W., Amazigo, J.C., 1967. Imperfection sensitivity of eccentrically stiffened cylindrical shells. AIAA Journal 5, 392–401.

Hutchinson, J.W., Frauenthal, J.C., 1969. Elastic postbuckling behavior of stiffened and barreled cylindrical shells. J. Appl. Mechanics 36, 784–790.

Ibrahimbegovic, A., 1994. Stress resultant geometrically nonlinear shell theory with drilling rotations—Part I: a consistent formulation. Comp. Meth. in Appl. Mech. and Engineering 118 (3–4), 265–284.

Ibrahimbegovic, A., Frey, F., 1994. Stress resultant geometrically nonlinear shell theory with drilling rotations—Part II: computational aspects. Comp. Meth. in Appl. Mech. and Engineering 118 (3–4), 285–308.

Kheyrkhahan, M., 1995. Postbuckling analysis and imperfection sensitivity of general shells by the finite element method. Ph.D. dissertation, University of Michigan, U.S.A.

Koiter, W.T., 1945. On the stability of elastic equilibrium. Dissertation, Delft, Holland (English translation issued as NASA, Tech. Trans. F-10, 833, 1967).

Peek, R., 1995. Postbuckling behavior and the worst imperfection shape for periodic structures, unpublished work.

Peek,R., Kheyrkhahan, M., 1993. Postbuckling behavior and imperfection sensitivity of elastic structures by the Lyapunov–Schmidt–Koiter approach. Comp. Meth. in Appl. Mech. and Engineering 108, 261–279.

Potier-Ferry, M., 1987. Foundations of elastic postbuckling theory. Buckling and postbuckling. In: Arbocz, J., Potier-Ferry, M., Singer, J., Tvergaard, V. (Eds.) Lecture notes in physics, vol. 288. Springer, Berlin, pp. 83–142.

Rizzi, N., Tatone, A., 1985. Symbolic manipulation in buckling and postbuckling analysis. Computers and Structures 21, 691–700.

Semenyuk, N. P., 1987. Stability of imperfectly cylindrical shells made from composite materials. Prikladnaya Mekhanika, 23, 37–43. (Translation in: Soviet Applied Mechanics, Plenum Publishing Corporation.)

Simo, J.C., Fox, D.D., 1989. On a stress resultant geometrically exact shell model. Part I: formulation and optimal parametrization. Comp. Meth. in Appl. Mech. and Engineering 72, 267–304.

Thompson, J.M.T., Hunt, G.W., 1973. A general theory of elastic stability. John Wiley, New York.

Triantafyllidis, N., Peek, R., 1992. On the stability and the worst imperfection shape in solids with nearly simultaneous eigenmodes. Int. J. Solids Structures 29, 2281–2299.

Vainberg, M.M., Trenogin, V.A., 1962. The methods of Lyapunov and Schmidt in the study of nonlinear equations and their further development. Russ. Math. Surveys 17, 1–60.

Wohlever, J.C., 1993. A group theoretic approach to the nonlinear bifurcation analysis of shells of revolution. Ph.D. dissertation, Cornell University, U.S.A.